Research Square

Preprints are preliminary reports that have not undergone peer review.
They should not be considered conclusive, used to inform clinical practice,
or referenced by the media as validated information.

Deep-Seated Mantle Plumes Detected Beneath the Moon's Earth-Facing Hemisphere

Jiaqi Li

lijiaqi315@gmail.com

Peking University https://orcid.org/0000-0001-7525-5401

Jing Shi

Peking University https://orcid.org/0000-0003-1147-0975

Nan Zhang

Peking University https://orcid.org/0000-0001-5160-5630

Article

Keywords:

Posted Date: August 21st, 2025

DOI: https://doi.org/10.21203/rs.3.rs-7377649/v1

License: This work is licensed under a Creative Commons Attribution 4.0 International License.
Read Full License

Additional Declarations: There is **NO** Competing Interest.

Deep-Seated Mantle Plumes Detected Beneath the Moon's Earth-Facing Hemisphere

Jing Shi[1], Nan Zhang[1], Jiaqi Li[1,*]

[1] SKLab-DeepMinE, MOEKLab-OBCE, School of Earth and Space Sciences, Peking University, Beijng, China.

*Corresponding author. Email: JLI@pku.edu.cn

Abstract

The Moon's mare basalts, which record over two billion years of lunar volcanic activity[1,2], hold key clues to the driving forces behind lunar magmatism. These igneous rocks are predominantly concentrated on the lunar nearside[3,4], giving rise to two competing hypotheses: one attributing the volcanism to shallow melting near the crust-mantle boundary[5,6], and the other to deep mantle upwellings[7,8] following an early mantle overturn[9,10]. However, in the absence of direct observational constraints on the deep structures of the Moon, the origin of this sustained, nearside-focused volcanism remains unresolved. Here, we present seismological evidence of deep thermal plumes beneath the lunar nearside today, revealing striking spatial correlations with surface enrichments in heat-producing elements. We propose that these plumes, likely originating from the core-mantle boundary, are remnants of post-overturn mantle dynamics that fuel mare volcanism. Our findings resolve the long-standing debate over the Moon's internal heat sources by revealing that persistent deep thermal plumes beneath the nearside bridge ancient mare volcanism and present-day mantle dynamics. For the first time, this result establishes a unified framework that connects spatial and temporal clues across the Moon's evolutionary history.

Main text

The Moon's surface today exhibits quiescent geological behavior, with no active volcanism and only rare shallow moonquakes, indicating minimal tectonic activity[3,11,12]. Dynamic processes are limited to a liquid outer core[13] and a thin, low-viscosity, partially molten layer above the core-mantle boundary (CMB)[13–18]. Beyond these regions, however, the dynamical state of the deep lunar interior, particularly the middle-

to-lower mantle, remains poorly constrained due to a lack of direct observational evidence, rendering its quiescence or activity a matter of assumption.

Lunar mare basalts, which predominantly cover the nearside, indicate a prolonged volcanic history of the Moon. These basalts, with ages peaking around 3.8 billion years ago (Ga)[19], point to a period of intense volcanic activity. Nonetheless, lunar volcanism appears to have extended much longer, with evidence of eruptions in ~2.0 Ga as indicated by Chang'e-5 samples[1,2]. The origin of this volcanism and its sustained activity remain debated.

Two competing hypotheses have been proposed to explain the origin of lunar mare basalts. One posits a shallow source, where melting initiates near the crust-mantle boundary and propagates downward, without invoking deep mantle plumes[5,6,20,21]. However, the other suggests a deep origin, involving mantle plumes rising from the core-mantle boundary (CMB), driven by concentrated heat-producing elements within ilmenite-rich cumulates[7,8,22,23]. These dense cumulates are believed to have settled above the CMB following mantle overturn early in the Moon's history[9,10]. To date, the absence of direct constraints has made it difficult to reconcile these divergent scenarios, which imply essentially different thermal, compositional, and structural evolutionary pathways for the Moon.

Resolving the mantle structures related to the post-overturn mantle is thus crucial for distinguishing competing models and explaining mare volcanism. As the missing piece of the puzzle, the structures of Moon's middle-to-lower mantle will bridge the quiescent surface with the active deep interior across space and time, unveiling the Moon's internal dynamics and long-term thermal evolution with unprecedented clarity.

Mantle plumes that once upwelled through the Moon's interior may have left behind deep-seated thermal plumes, sustained by radiogenic heating within the deep mantle or by external tidal energy from the Earth[8,23]. Such plumes are expected to modulate seismicity distribution: elevated temperatures promote the plastic deformation of rocks, thereby inhibiting seismic ruptures, as is well documented in terrestrial analogues[24–26]. Additionally, increased temperatures enhance seismic attenuation, causing preferential damping of high-frequency seismic energy, whereas low-frequency portions persist[27,28]. The numerous deep moonquakes recorded during the Apollo missions[11,12,29] provide an opportunity to explore these features.

In this study, we identify deep thermal plumes beneath the Moon's nearside through three diagnostic signatures: seismicity gaps; pronounced seismic attenuation; and correlated enrichments of surface heat-producing elements. Together with other observational data, these plumes provide, for the first time, a coherent framework linking the Moon's present-day surface and deep structures to its past and ongoing thermal evolution.

Seismicity gaps in deep moonquakes

Using all published deep moonquake catalogs[30–34] derived from various methods, velocity models, and independent datasets, we mapped the locations of deep moonquakes on the lunar nearside (**Fig. 1a**). Two prominent seismicity gaps appear near the center of the Apollo seismic array, even accounting for location uncertainties. One gap lies northwest of the center (from around $2°N$ to $30°N$, $25°W$ to $5°E$), and the other lies to its south (from around $5°S$ to $25°S$, $8°W$ to $8°E$). We conservatively outlined these two gaps as red zones in **Fig. 1b**, incorporating the estimated positioning errors of deep moonquakes.

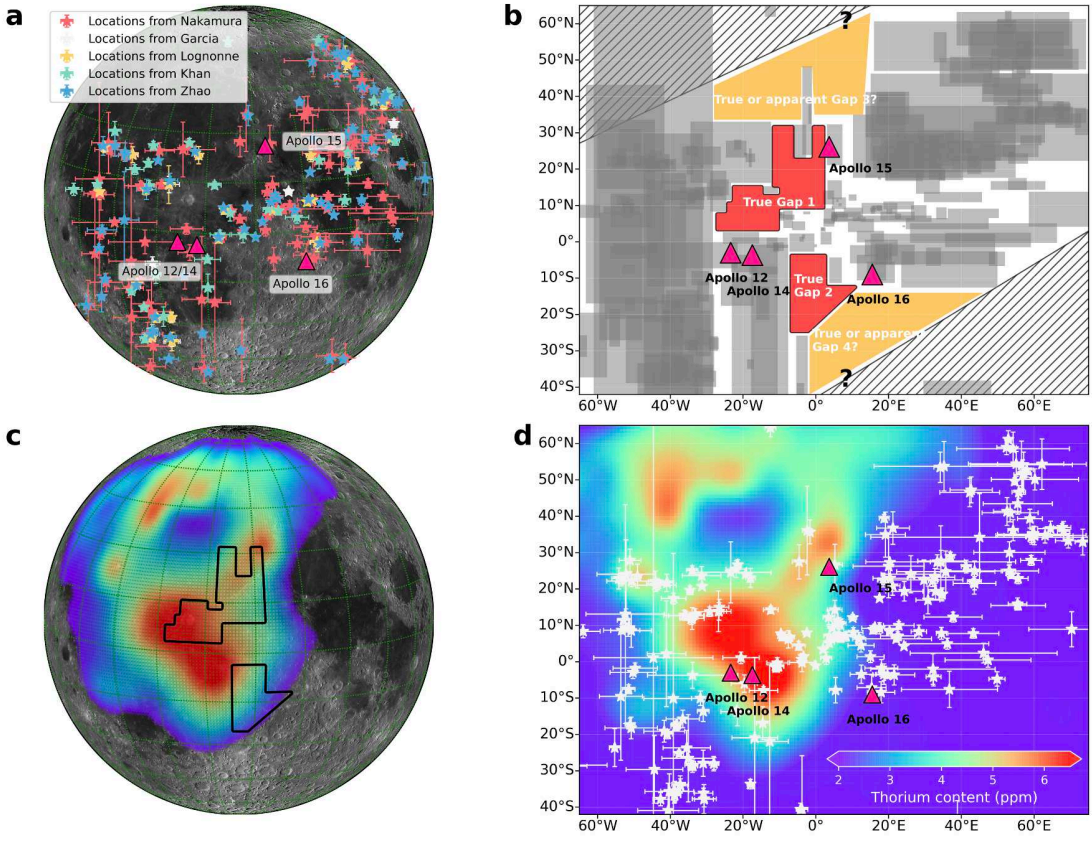


Fig. 1 | Seismicity gaps in deep moonquakes and their association with the distribution of thorium, a heat-producing element. a, Distribution of deep moonquakes on the lunar nearside. Stars denote the locations of deep moonquakes from independent studies (colour-coded), with error bars indicating positional uncertainties[30–34]. Pink triangles mark the deployment sites of the Apollo seismometers. The lunar map[35] is projected in an orthographic manner. **b**, Seismicity gaps in deep moonquake distribution. Gray transparent areas show all possible source regions of deep moonquakes. Each gray transparent box is centered on the corresponding event location, with side lengths scaled to location errors. The darker the colour, the greater the number of deep moonquakes. Red-filled polygons delineate two confirmed seismicity gaps (i.e., true gaps) within the coverage of the Apollo seismic array. Orange-filled polygons indicate potential gaps (i.e., true or apparent gaps) outside the array. Diagonal shading denotes regions with reduced detection capability due to array geometry constraints. Question marks indicate inferred

detection boundaries. **c**, Two confirmed seismicity gaps (black polygons) superimposed on the surface distribution of thorium abundance[36]. For clarity, only the distribution of thorium above 2 ppm is shown. **d**, The distribution of deep moonquakes (white stars, identical to panel **a**) overlays the lunar thorium abundance map[36]. The color bar is shared by both panels **c** and **d**, representing the abundance of thorium.

Three lines of evidence indicate that the two seismicity gaps are genuine rather than artifacts. Firstly, deep moonquake events, located within the triangular array of Apollo stations, have the highest location accuracy, as demonstrated by nearby events with small uncertainties. Secondly, the same gaps appear consistently across five different location catalogs that use different datasets and algorithms[30–34], ruling out data and methodological bias. Thirdly, synthetic tests demonstrate that if events had occurred within the two gaps, they could have been reliably located using arrival times from as few as two Apollo stations (**Supplementary Information section 1**).

In addition to the two robust seismicity gaps, we identified two other areas without seismicity, which are shown in orange zones in **Fig. 1b**. However, because they fall outside the Apollo array, it is unclear whether they represent genuine seismicity gaps or are the result of limitations in observational coverage. We also note the presence of several smaller candidate gaps, but due to their limited spatial extent, they are not considered further in this study.

Importantly, we emphasized that two genuine seismicity gaps (the red regions in **Fig. 1b**) are clearly present within the four-station Apollo network. Such seismicity gaps may indicate regions of increased plasticity[37] in the lunar interior, which would inhibit the occurrence of deep moonquakes. Since deep moonquakes originate at depths of 700 – 1,200 km[30–34], any thermal anomaly that enhances rock plasticity is likely to be situated near the CMB.

Regions of pronounced seismic attenuation

If deep-seated thermal anomalies are present, they should cause significant attenuation of seismic energy, which may be detectable in deep moonquake waveforms. To test this hypothesis, we analyzed stacked waveforms of deep moonquakes with well-constrained locations. These refer to events whose locations are confirmed and consistent across at least four independent studies (see **Extended Data Fig. 1**). The clustered and repeatable nature of deep moonquakes enables waveform stacking to enhance the signal-to-noise ratio (SNR) of deep moonquake waveforms[11,38,39]. In order to minimize potential artifacts from the stacking procedures, we used three independent datasets (**Extended Data Fig. 2 – 4**) compiled by different researchers[40].

Seismic attenuation preferentially reduces the high-frequency components of seismic energy, producing low-frequency signals with well-separated cycles that can be

distinguished visually[27,28] (e.g., red lines in **Fig. 2b, 2e, 2h**). In contrast, the high-frequency waveforms contain more short-period energy, leading to more intense and compressed waveforms (e.g., blue lines in **Fig. 2b, 2e, 2h**).

To quantify this effect, we introduced the spectral ratio (R) value, defined as $R = HF/BF$, which is the ratio of the high-frequency component (HF) in the waveform's amplitude spectrum to the broader frequency component (BF) (see Methods). Strong seismic attenuation damps high-frequency energy, lowering spectral ratio values.

We measured the spectral ratio of the direct S wave from deep moonquakes. As the direct S wave propagates directly from the source to the station, it is highly sensitive to the attenuation characteristic along its propagation path. It is also the most prominent phase in deep moonquake waveforms[38,41]. We used stacked waveforms recorded by the Apollo 12, Apollo 15, and Apollo 16 stations. Data from Apollo 14 were excluded due to a pronounced site effect near 0.9 Hz[42,43], which could bias the analysis of the frequency content.

Factors that can influence the spectral ratio value include site effects near the station, source-side effects, and path effects. Three converging arguments suggest that strong seismic attenuation occurs along specific propagation paths and is concentrated within the two seismicity gaps outlined in red zones in **Fig. 1b**.

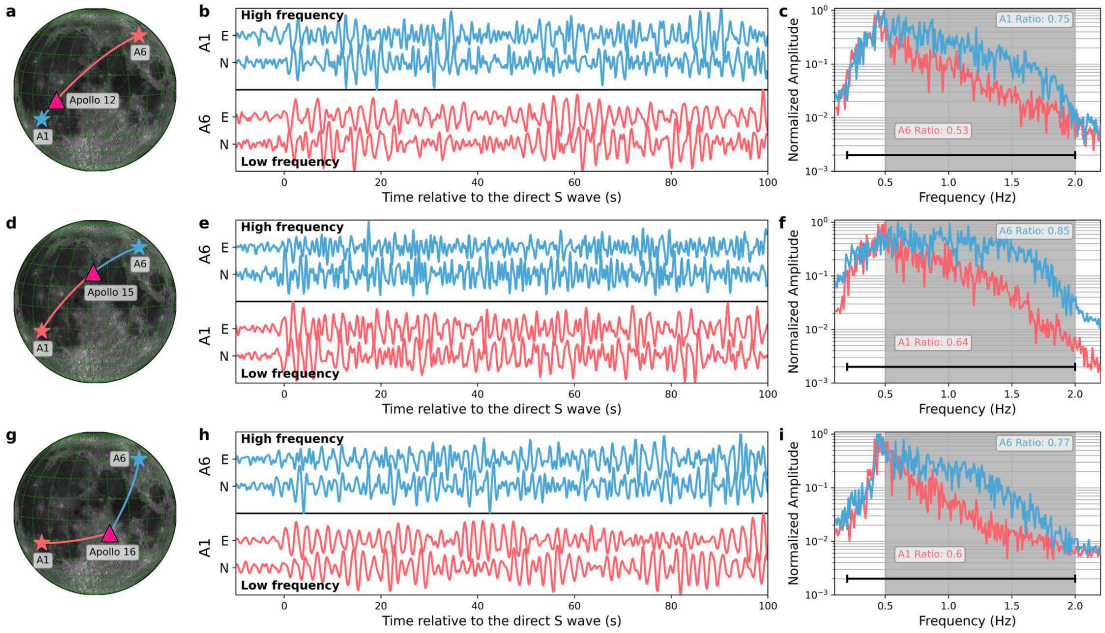


Fig. 2 | Representative Low- and High-frequency deep moonquake waveforms and amplitude spectra recorded by the Apollo 12 (a – c), Apollo 15 (d – f), and Apollo 16 (g – i) stations, shown for comparison. a, d, g, Raypaths for selected station-event pairs. The pink triangle indicates the location of the corresponding Apollo station. Red and blue stars mark the locations of events classified as relatively Low- and High-frequency, respectively, based on the waveforms recorded at each station. Coloured lines represent the S-wave raypaths from each event to its recording station. The line colours correspond to the stars, with red indicating

relatively Low-frequency and blue indicating relatively High-frequency events. **b, e, h**, Stacked waveforms of deep moonquakes. The stacked waveforms were compiled by Yosio Nakamura (available in ref.40) and bandpass filtered between 0.05 and 2.5 Hz. Red and blue lines indicate relatively Low- and High-frequency waveforms, respectively. Event names and the northern (N)- and eastern (E)-component labels are shown along the Y-axis. The X-axis denotes the time relative to the direct *S*-wave arrival. **c, f, i**, Normalized amplitude spectra of the corresponding events. The red and blue curves represent the average amplitude spectra of the two horizontal components for the Low-frequency and High-frequency events, respectively. The spectral ratio of each event is indicated in the lower left and upper right corners. Spectral ratios were computed as the energy in the high-frequency band (0.5 – 2.0 Hz; shaded gray box) divided by that in the broader band (0.2 – 2.0 Hz; black horizontal line).

At the same station, the spectral ratios of direct *S* waves from different deep moonquakes are clearly distinct. Based on their spectral ratios, events can be grouped into relatively Low- and High-frequency categories at each station. **Fig. 2** presents representative examples of relatively Low- and High-frequency deep moonquakes recorded at each station. The contrast between these two types of events is obviously reflected in both their waveform characteristics (**Fig. 2b, 2e, 2h**) and spectral ratios (**Fig. 2c, 2f, 2i**). The variability in spectral ratios among events observed at the same station suggests that these differences are not attributable to local site effects.

For the same event, different stations yield distinct spectral ratios. For example, the waveforms from event A1 are classified as the High-frequency event at Apollo 12 ($R = 0.75$), but as the Low-frequency at Apollo 15 and Apollo 16, where the spectral ratio values are below 0.65 (**Fig. 2c, 2f, 2i**). Although absolute spectral ratio values may not be directly comparable across stations due to differing site effects, analysis of the horizontal-to-vertical spectral ratio indicates that Apollo 12 tends to amplify low-frequency energy, whereas Apollo 15 and Apollo 16 enhance high-frequency components[43]. In theory, site effects should cause the lowest spectral ratios at Apollo 12 among the three stations, which contradicts the observations. This discrepancy further rules out local site effects as the primary cause of the spectral differences. Therefore, the variation in spectral ratios for the same event across different stations suggests that the observed spectral differences do not originate near the source.

The relative frequency content of deep moonquake waveforms recorded at each station is raypath dependent. For Apollo 12 (**Extended Data Fig. 5a – 5c**), events originating northeast and north of the station exhibit relatively Low-frequency waveforms, while those from the southwest appear relatively High-frequency (e.g., A6: 0.53 versus A1: 0.75 in **Fig. 2c**). For Apollo 15 (**Extended Data Fig. 5d – 5f**), events from the southwest and south yield Low-frequency waveforms, whereas those from the west and east have a higher frequency (e.g., A1: 0.64 versus A6: 0.85 in **Fig. 2f**). At Apollo 16

(**Extended Data Fig. 5g – 5i**), waveforms from the west are relatively Low-frequency, while those from the northeast are relatively High-frequency (e.g., A1: 0.60 versus A6: 0.77 in **Fig. 2i**). All three independent stacked waveform datasets consistently show these patterns.

This trend persists across a range of parameter choices, including the use of only high-SNR waveforms and variations in the time window or frequency band employed for spectral ratio calculations (Methods; **Extended Data Fig. 6 – 9**). While the relative spectral ratios of individual events may fluctuate, the overall pattern remains consistent. Station-event pairs with stable spectral classifications under different parameter settings were retained, and their corresponding waveforms were shown in **Extended Data Fig. 10 – 12**. For each of the three stations, the raypaths of events classified as relatively Low- or High-frequency were projected onto the lunar surface (**Fig. 3a – 3c**).

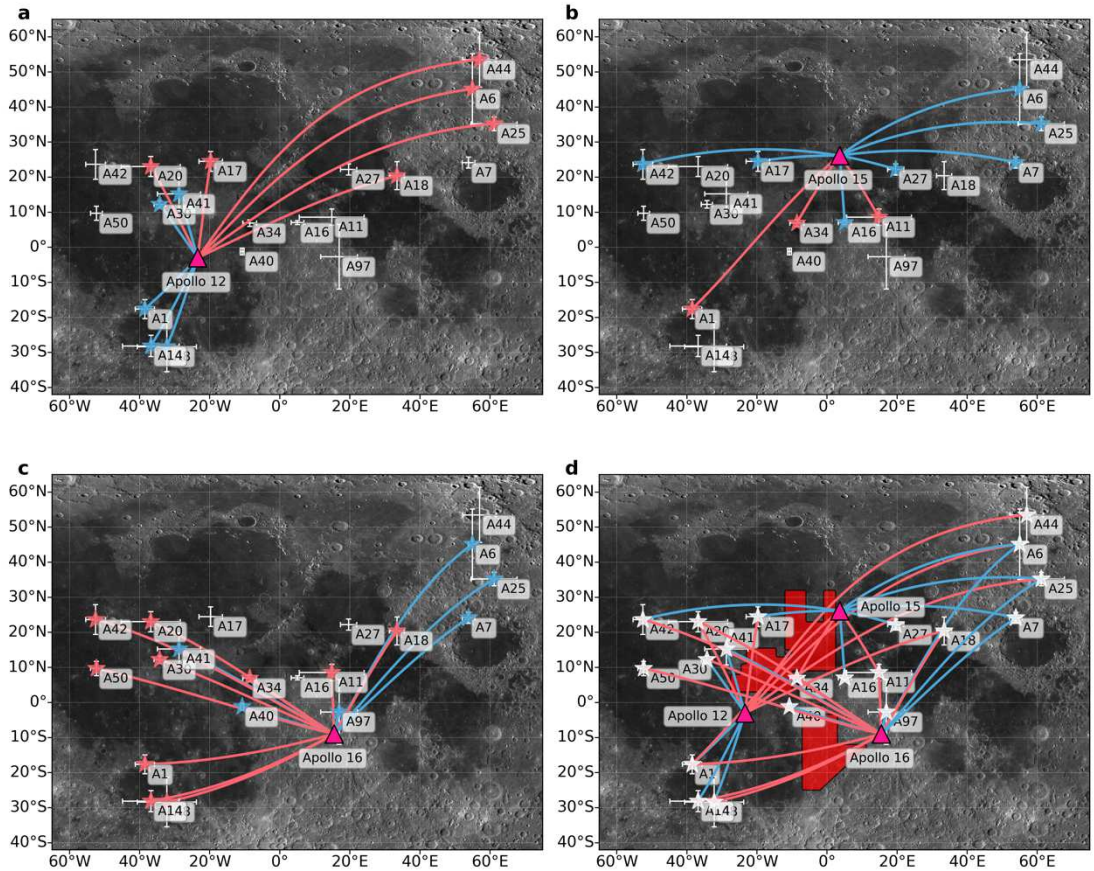


Fig. 3 | Raypath projections of relatively Low- and High-frequency deep moonquakes recorded at the Apollo 12 (a), Apollo 15 (b), and Apollo 16 (c) stations. a,b,c, White crosses with error bars mark events with well-constrained locations (see **Extended Data Fig. 1**), and event names are labelled accordingly. Red stars and raypaths denote relatively Low-frequency events, and blue stars and raypaths denote relatively High-frequency events. Some events marked with white crosses lack projected raypaths due to either their low signal-to-noise ratios or inconsistent spectral classifications under varying analysis parameters (see Methods). **d**,

Combined projection of raypaths for all retained station-event pairs. The red polygon marks the seismicity gap regions outlined in **Fig. 1**.

Regions of pronounced seismic attenuation coincide with the seismicity gaps, as can be clearly observed on the map showing all projected raypaths (**Fig. 3d**). Raypaths that propagate through these two seismicity gaps are associated with relatively Low-frequency waveforms (red lines in **Fig. 3d**), whereas those that avoid these regions exhibit relatively High-frequency characteristics (blue lines **Fig. 3d**). A few exceptions exist, which may result from uncertainties in event locations or some smalle thermal anomalies. Examining unstacked waveforms reinforces this raypath-dependent distribution of frequency characteristics among different events (Methods; **Extended Data Fig. 20**), although the number of stable classifications for station-event pairs decreases due to the generally low SNRs for unstacked waveforms.

Surface heat-producing element correlations

The spatial correlation between seismicity gaps and regions of strong seismic attenuation in deep moonquakes reveals deep thermal anomalies, which align with surface enrichments of heat-producing elements, identifying them as deep thermal plumes.

The nearside mare is characterized by an elevated concentration of heat-producing elements[5,36,44], such as uranium, thorium, and potassium, compared to other lunar regions. Notably, the highest thorium concentrations (> 6 ppm) are found around $10°N$, $20°W$ (**Fig. 1c, 1d**), aligning closely with the first conservatively estimated seismicity gap (true gap 1; **Fig. 1b, 1c**) and marginally matching the second one (true gap 2).

Randomness tests demonstrate that the reduced seismic activity within regions enriched in heat-producing elements is not a random occurrence. For deep moonquakes located within regions with thorium concentrations greater than 6 ppm, five independent event catalogs[30–34] yield proportions of 2.29%, 1.15%, 1.15%, 1.15%, and 1.14%, respectively. In comparison, 10,000 Monte Carlo simulations, randomly distributing the same number of events within the detectable area of **Fig. 1b,** produce an average probability of ~3.30% (**Extended Data Fig. 21**), which exceeds all observed values. Even at a lower threshold of 5 ppm, the simulated mean proportion of ~8.90% remains higher than all the observed values of 5.71%, 2.30%, 2.30%, 3.45%, and 2.86% (**Extended Data Fig. 22**).

These results demonstrate that the paucity of deep moonquakes in thorium-rich regions is statistically significant and unlikely to be due to chance. This spatial anti-correlation suggests a genetic relationship between the seismicity gaps and the enriched surface heat-producing elements. The close alignment between the seismicity gap 1 and the

enriched heat-producing elements suggests that deep interior processes have contributed to the surface enrichment, even if part of heat-producing elements may originate from the Imbrium impact[45]. Additional support for a deep contribution comes from the non-concentric distribution of high thorium abundances around the Imbrium basin and the elevated thorium levels observed at the relatively young Copernicus crater (around $9.5°N,\ 20°W$). Thus, past mantle upwellings contribute to the high-producing elements at the surface.

Present-day deep thermal plumes

The strong seismic attenuation in the regions lacking deep moonquake seismicity indicates the presence of at least two compelling thermal plumes beneath the lunar nearside (outlined in red regions in **Fig. 1b**). Deep moonquakes originate at depths of 700 – 1,200 km[30–34], so these thermal plumes are deep-seated and originate near the CMB. Furthermore, they must lie below ~650 km, as the direct *S*-wave raypaths of all identified Low-frequency events to their corresponding stations intersect the Moon's interior only down to this depth (**Extended Data Fig. 23**).

The gravity-based tidal response can also be used to infer the deep thermal plumes. Specifically, deep thermal plumes beneath the nearside may alter the Moon's tidal response and, consequently, its gravitational field. Ref.46 reports a third-degree Love number (k_3) of 0.0163 ± 0.0007 for the Moon, implying a 2 – 3% difference in shear modulus in the deep mantle (below ~600 km) between hemispheres. However, due to the limited spatial resolution of the Love number inversion, the anomaly was attributed to an average temperature difference of $100 – 200\ K$ between the two hemispheres, and its exact location remained unconstrained. We suggest that the deep thermal anomaly inferred from the k_3 actually corresponds to the nearside thermal plumes.

The deep plumes observed in this study confirm the one-sided thermochemical anomalies near the CMB predicted by geodynamics[7,8,22,23]. Some geodynamical simulations show that, following mantle overturn, radiogenic heating from the ilmenite cumulates would trigger the melting of mantle materials and drive buoyant upwelling towards the surface[7,8]. This mechanism can explain the widespread mare volcanism that occurred between ~3.3 and 3.8 Ga[19] **(Extended Data Fig. 24; Fig. 4a**), as well as the operation of a short-lived core dynamo[22]. The remaining ilmenite deposits will remain near the CMB, forming deep thermochemical anomalies beneath the nearside[7,8]. Elevated concentrations of heat-producing elements within the seismicity gap 1 reflect the surface manifestations of these once-active mantle upwellings **(Fig. 4b**). Their thermal remnants persist in the middle-to-lower mantle as the deep thermal plumes identified here (**Fig. 4c**), supporting that the one-sided thermochemical structures[7,8,22] are the result of the long-term thermal evolution of the Moon. In comparison, the

seismicity gap 2 is adjacent to the thorium-rich region (**Fig. 1c**). This may reflect the inclined geometry of a past underlying mantle upwelling, or alternatively, it is located at the boundary between mare and highland terrains, where past upwellings beneath have not reached the surface.

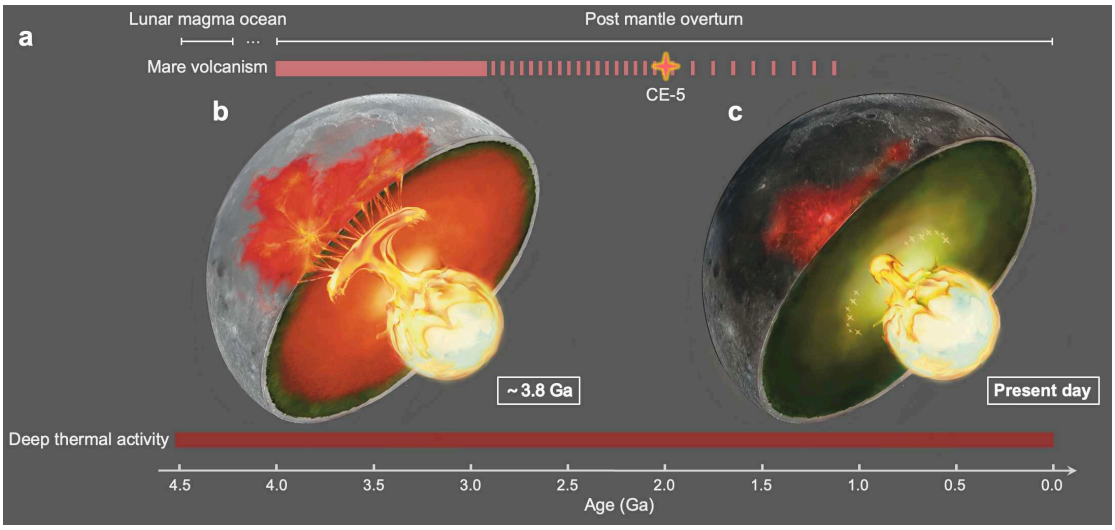


Fig. 4 | Schematic illustration of the Moon's interior structure and thermal evolution. a, Temporal evolution of the Moon. Two horizontal white lines at the top mark the lunar magma ocean phase and the subsequent mantle overturn period, respectively; the dots between denote the mantle overturn stage. The light red shading indicates the duration and intensity of lunar mare volcanism, with continuity reflecting volcanic vigor (modified from ref.47). The red star marks the ~2.0 Ga age determined from Chang'e-5 samples. The dark red band at the base represents sustained deep thermal activity, revealed by this study to persist from lunar formation to the present. The bottom arrow denotes the timeline in billion years ago (Ga), progressing from right to left. **b**, Conceptual model of mantle upwelling around 3.8 Ga. Thermal upwelling originates at the core-mantle boundary, driven by internal heat from overturned ilmenite-rich material. The plume ascends to the shallow mantle[48], inducing partial melting and ultimately generating the mare basalts observed at the surface. **c**, Present-day schematic of the lunar interior. Deep thermal plumes, preserved as remnants of past mantle upwellings, coincide with seismicity gaps and align with surface enrichments in heat-producing elements (red areas). Yellow stars represent deep moonquakes.

The presence of persistent thermal plumes in the Moon suggests that it experiences long-lived magmatic activity. This explains the young (~2.0 Ga) basalts sampled by Chang'e-5[1,2]. Recent dynamical models demonstrate that, in addition to radiogenic heating, tidal dissipation driven by Earth's gravitational pull provides a sustained external heat source for the Moon[23], supporting the plausibility of deep-seated thermal plumes. This tidal influence is further evidenced by the periodic triggering of deep moonquakes[39,49].

This study, for the first time, presents the direct observational constraints that integrate the spatial and temporal evolution of the Moon following mantle overturn within a

consistent framework (**Fig. 4**). Spatially, we reveal that deep thermal plumes persist today between the dormant lunar surface and the active deep interior. Their locations coincide with surface enrichments in heat-producing elements, thereby linking the deep mantle upwellings with the formation of mare basalts[7,8,22]. Temporally, the survival of these plumes into the present connects the Moon's prolonged mare volcanism to deep interior processes, offering a plausible heat source for the young basaltic eruptions observed in Chang'e-5 samples[1,2]. Together, the thermal plumes identified in this paper reconcile long-standing observational and theoretical puzzles, and establish a missing link between surface geology and mantle dynamics, marking a major step forward in our understanding of the Moon's interior evolution.

References

1. Che, X. *et al.* Age and composition of young basalts on the Moon, measured from samples returned by Chang'e-5. *Science* **374**, 887–890 (2021).
2. Li, Q.-L. *et al.* Two-billion-year-old volcanism on the Moon from Chang'e-5 basalts. *Nature* **600**, 54–58 (2021).
3. Jolliff, B. L., Wieczorek, Mark. A., Shearer, C. K. & Neal, C. R. *New Views of the Moon*. vol. 60 (Mineralogical Society Of America Geochemical Society, 2006).
4. Head, J. W. & Wilson, L. Lunar mare volcanism: Stratigraphy, eruption conditions, and the evolution of secondary crusts. *Geochimica et Cosmochimica Acta* **56**, 2155–2175 (1992).
5. Wieczorek, M. A. & Phillips, R. J. The "Procellarum KREEP Terrane": Implications for mare volcanism and lunar evolution. *J. Geophys. Res.* **105**, 20417–20430 (2000).
6. Laneuville, M., Wieczorek, M. A., Breuer, D. & Tosi, N. Asymmetric thermal evolution of the Moon: LUNAR EVOLUTION. *J. Geophys. Res. Planets* **118**, 1435–1452 (2013).
7. Zhong, S., Parmentier, E. M. & Zuber, M. T. A dynamic origin for the global asymmetry of lunar mare basalts. *Earth and Planetary Science Letters* **177**, 131–140 (2000).
8. Zhang, N., Parmentier, E. M. & Liang, Y. A 3-D numerical study of the thermal evolution of the Moon after cumulate mantle overturn: The importance of rheology and core solidification: 3-D MANTLE AND 1-D CORE LUNAR EVOLUTION. *J. Geophys. Res. Planets* **118**, 1789–1804 (2013).
9. Kesson, S. E. & Ringwood, A. E. Mare basalt petrogenesis in a dynamic moon. *Earth and Planetary Science Letters* **30**, 155–163 (1976).
10. Zhang, N. *et al.* Lunar compositional asymmetry explained by mantle overturn following the South Pole–Aitken impact. *Nat. Geosci.* 37–41 (2022)

doi:10.1038/s41561-021-00872-4.
11. Nakamura, Y., Latham, G. V. & Dorman, H. J. Apollo Lunar Seismic Experiment—Final summary. *J. Geophys. Res.* **87**, A117 (1982).
12. Garcia, R. F. *et al.* Lunar Seismology: An Update on Interior Structure Models. *Space Sci Rev* **215**, 50 (2019).
13. Weber, R. C., Lin, P.-Y., Garnero, E. J., Williams, Q. & Lognonné, P. Seismic Detection of the Lunar Core. *Science* **331**, 309–312 (2011).
14. Harada, Y. *et al.* Strong tidal heating in an ultralow-viscosity zone at the core–mantle boundary of the Moon. *Nature Geosci* **7**, 569–572 (2014).
15. van Kan Parker, M. *et al.* Neutral buoyancy of titanium-rich melts in the deep lunar interior. *Nature Geosci* **5**, 186–189 (2012).
16. Briaud, A., Ganino, C., Fienga, A., Mémin, A. & Rambaux, N. The lunar solid inner core and the mantle overturn. *Nature* **617**, 743–746 (2023).
17. Khan, A., Connolly, J. A. D., Pommier, A. & Noir, J. Geophysical evidence for melt in the deep lunar interior and implications for lunar evolution. *J. Geophys. Res. Planets* **119**, 2197–2221 (2014).
18. Qin, C., Muirhead, A. C. & Zhong, S. Correlation of deep moonquakes and mare basalts: Implications for lunar mantle structure and evolution. *Icarus* **220**, 100–105 (2012).
19. Hiesinger, H., Head, J. W., Wolf, U., Jaumann, R. & Neukum, G. Ages and stratigraphy of lunar mare basalts: A synthesis. in *Recent Advances and Current Research Issues in Lunar Stratigraphy* (Geological Society of America, 2011). doi:10.1130/2011.2477(01).
20. Elardo, S., Cone, K., Williams, S., Siegler, M. A. & Palin, R. M. A shallow mantle source for the Chang'e 5 lavas reveals how top-down heating prolonged lunar magmatism. *Science Advances* **11**, eadr1486 (2025).
21. Tian, H.-C. *et al.* Surges in volcanic activity on the Moon about two billion years ago. *Nat Commun* **14**, (2023).
22. Stegman, D. R., Jellinek, A. M., Zatman, S. A., Baumgardner, J. R. & Richards, M. A. An early lunar core dynamo driven by thermochemical mantle convection. *Nature* **421**, 143–146 (2003).
23. Zhang, W. & Zhang, N. Long-lived lunar mare volcanism powered by radiogenic and tidal heating. in P22A-05 (2023).
24. Parnell-Turner, R. Earthquake Seismicity Reveals the Location and Significance of the Shona Mantle Plume in the South Atlantic Ocean. *Geophysical Research Letters* **51**, e2024GL109738 (2024).
25. Schlindwein, V., Demuth, A., Geissler, W. H. & Jokat, W. Seismic gap beneath Logachev Seamount: Indicator for melt focusing at an ultraslow mid-ocean ridge?

Geophysical Research Letters **40**, 1703–1707 (2013).
26. Parnell-Turner, R. E. *et al.* Crustal manifestations of a hot transient pulse at 60°N beneath the Mid-Atlantic Ridge. *Earth and Planetary Science Letters* **363**, 109–120 (2013).
27. Abbas, A., Yang, H. & Zi, J. Deciphering the low-frequency seismic signals in the Weiyuan Shale gas field: implications for reservoir and structural heterogeneity. *Geophysical Journal International* **237**, 109–122 (2024).
28. Hicks, S. P. *et al.* Slab to back-arc to arc: Fluid and melt pathways through the mantle wedge beneath the Lesser Antilles. *SCIENCE ADVANCES* (2023).
29. Lognonné, P. Planetary seismology. *Annu. Rev. Earth Planet. Sci.* **33**, 571–604 (2005).
30. Nakamura, Y. Farside deep moonquakes and deep interior of the Moon. *J. Geophys. Res.* **110**, E01001 (2005).
31. Lognonné, P., Gagnepain-Beyneix, J. & Chenet, H. A new seismic model of the Moon: implications for structure, thermal evolution and formation of the Moon. *Earth and Planetary Science Letters* **211**, 27–44 (2003).
32. Garcia, R. F., Gagnepain-Beyneix, J., Chevrot, S. & Lognonné, P. Very preliminary reference Moon model. *Physics of the Earth and Planetary Interiors* **188**, 96–113 (2011).
33. Khan, A. & Mosegaard, K. An inquiry into the lunar interior: A nonlinear inversion of the Apollo lunar seismic data. *J. Geophys. Res.* **107**, 5036 (2002).
34. Zhao N., Zhu P., Zhang B. & Yuan Y. Moonquake Relocation. *Eart. Scie.* **40**, 1276 (2015).
35. Robinson, M. LRO MOON LROC 5 RDR V1.0, LRO-L-LROC-5-RDR-V1.0, NASA Planetary Data System (PDS). (2019) doi:10.17189/1520341.
36. Yamashita, N. *et al.* Uranium on the Moon: Global distribution and U/Th ratio: URANIUM ON THE MOON. *Geophys. Res. Lett.* **37**, n/a-n/a (2010).
37. Mia, M. S., Abdelmeguid, M. & Elbanna, A. E. Spatio-Temporal Clustering of Seismicity Enabled by Off-Fault Plasticity. *Geophysical Research Letters* **49**, e2021GL097601 (2022).
38. Nakamura, Y. New identification of deep moonquakes in the Apollo lunar seismic data. *Physics of the Earth and Planetary Interiors* **139**, 197–205 (2003).
39. Lammlein, D. R. Lunar seismicity and tectonics. *Physics of the Earth and Planetary Interiors* **14**, 224–273 (1977).
40. Nunn, C. *et al.* Lunar Seismology: a data and instrumentation review - Electronic Supplement. https://doi.org/10.5281/zenodo.7787610 (2020).
41. Bulow, R. C. New events discovered in the Apollo lunar seismic data. *J. Geophys. Res.* **110**, E10003 (2005).

42. Dal Moro, G. Joint analysis of Rayleigh-wave dispersion and HVSR of lunar seismic data from the Apollo 14 and 16 sites. *Icarus* **254**, 338–349 (2015).
43. Amrouche, M., Weber, R. C., Schmerr, N. & Iqbal, W. Effects of Lunar Near-Surface Geology on Moonquakes Ground Motion Amplification. *JGR Planets* **127**, e2022JE007396 (2022).
44. Gillis, J. J., Jolliff, B. L. & Korotev, R. L. Lunar surface geochemistry: Global concentrations of Th, K, and FeO as derived from lunar prospector and Clementine data. *Geochimica et Cosmochimica Acta* **68**, 3791–3805 (2004).
45. Levin, J. N., Evans, A. J., Andrews-Hanna, J. C. & Daubar, I. J. Lunar Crustal KREEP Distribution. *JGR Planets* **130**, e2024JE008418 (2025).
46. Park, R. S. *et al.* Thermal asymmetry in the Moon's mantle inferred from monthly tidal response. *Nature* 1188–1192 (2025) doi:10.1038/s41586-025-08949-5.
47. Mitchell, R. N. Chang'E-5 reveals the Moon's secrets to a longer life. *The Innovation* **2**, 100177 (2021).
48. Wieczorek, M. A. *et al.* The Constitution and Structure of the Lunar Interior. *Reviews in Mineralogy and Geochemistry* **60**, 221–364 (2006).
49. Kawamura, T., Lognonné, P., Nishikawa, Y. & Tanaka, S. Evaluation of deep moonquake source parameters: Implication for fault characteristics and thermal state: Evaluation of DMQ Source Parameters. *J. Geophys. Res. Planets* **122**, 1487–1504 (2017).

Methods

Spectral ratio calculation

To calculate spectral ratios from stacked waveforms of deep moonquakes with well-constrained locations, we followed a four-step procedure.

Firstly, waveform preprocessing. Linear trends and mean values were removed from all waveforms, after which a 0.05 – 2.5 Hz Butterworth bandpass filter was applied. The two horizontal components were then corrected to the geographic northern and eastern directions, based on the azimuthal orientation of each Apollo seismic station[50].

Secondly, direct *S*-wave picking. The arrival time of the direct *S* wave, which is the most prominent phase in deep moonquake waveforms[38,41], was manually identified on each stacked trace (**Extended Data Fig. 2 – 4**). Three independent stacked waveform datasets[40] compiled by Yosio Nakamura, Philippe Lognonné, and Renee C. Bulow were adpoted. As our analysis uses a long time window, precise arrival-time picking is not required; the window length is sufficient to accommodate the typical uncertainties of *S*-wave arrival times. If the waveform quality is too poor or if no stacked waveform is

available in a given dataset, the arrival time of the direct *S* wave cannot be identified and the corresponding event is excluded from further analysis.

Thirdly, the frequency-domain transformation. Waveforms within the time window spanning 10 s before to 100 s after the picked *S*-wave arrival were extracted and transformed into the frequency domain using the Fourier transform. We computed the amplitude spectra of the two horizontal components, averaged them, and normalized the result by its maximum value to obtain the *S*-wave amplitude spectrum for each deep moonquake. Averaging the two components mitigates potential bias introduced by scattering effects.

Fourthly, the spectral ratio calculation. The spectral ratio ($R = HF/BF$) is defined as the ratio of high-frequency energy (HF; 0.5 – 2.0 Hz) to broader energy (BF; 0.2 – 2.0 Hz). The lower bound of 0.5 Hz for the high-frequency band was chosen to avoid the influence of the Apollo seismometer's peak response near 0.45 Hz[50]. The lower bound of 0.2 Hz for the broadband window excludes potential contamination from long-period instrumental noisy or thermal effects[51]. The upper limit of 2.0 Hz was selected because signal energy above this frequency is negligible.

Finally, **Extended Data Fig. 5** illustrates the distribution of spectral ratios measured from the three independent stacked waveform datasets.

Sensitivity test of the relative spectral ratio

In order to assess the effect of the choice of *S*-wave window length, frequency band, and waveform dataset on the relative spectral ratios of different events at the same station, we selected waveforms with high signal-to-noise ratios (SNRs) and systematically tested a range of parameter settings.

Specifically, we first excluded the potential influence of noise-induced artifacts on low-SNR *S* waves. For each stacked waveform dataset, we calculated the SNR of the direct *S* wave using the following equation:

$$SNR = 10 \cdot log_{10}\left(\frac{A_S}{A_N}\right)^2,$$

in which A_S and A_N are the root mean square amplitudes of the signal and noise, measured within 100-s window after and 50-s window before the direct *S*-wave arrival, respectively. We only retained events with an average SNR greater than 6.0 dB across both horizontal components, since the arrival time of the direct *S* wave becomes somewhat less reliable below this threshold. For each event with high-SNR waveforms being available in two or three stacked datasets, the spectral ratios were calculated for each waveform and were then averaged to produce the mean spectral ratio for that event. This averaging is justified by consistent patterns of relative spectral ratios across

different events recorded at the same station in all three independent datasets (**Extended Data Fig. 5**).

Subsequently, we tested four parameter combinations to evaluate the stability of the relative spectral ratio distributions across events at each station. **Extended Data Fig. 6 – 8** use a frequency band of 0.2 – 2.0 Hz with *S*-wave windows of 10 s before to 50 s, 100 s, and 150 s after the arrival, respectively. **Extended Data Fig. 9** uses a narrower band of 0.2 – 1.0 Hz with a -10 – 110 s window. In all cases, the overall patterns of spectral ratios are generally consistent.

After excluding station-event pairs with unstable spectral classifications under varying parameter settings, the following paris exhibit consistent spectral characteristics. At Apollo 12, relatively Low-frequency events include A6, A17, A18, A20, A25, and A44, while relatively High-frequency events include A1, A8, A14, A30, and A41. At Apollo 15, relatively Low-frequency events are A1, A11, and A34, while relatively High-frequency events are A6, A7, A16, A17, A25, A27, and A42. At Apollo 16, relatively Low-frequency events include A1, A8, A11, A14, A18, A20, A30, A34, A42, and A50, and relatively High-frequency events include A6, A7, A25, A40, A41, and A97. **Extended Data Fig. 10 – 12** show the *S*-wave waveforms for all of these station-event pairs in three independent stacked waveform datasets.

Spectral ratio calculation for unstacked waveforms

To further rule out the possibility that differences in spectral ratios among events arise from variations in the mode-dependent response of Apollo seismometers[50], we analyzed unstacked waveforms by removing instrumental responses.

For each deep moonquake with both reliable location information and high signal-to-noise ratio (SNR), we first retrieved waveform data from the Incorporated Research Institutions for Seismology (i.e., IRIS)[52], using the *levent.1008c* catalog[40] of deep moonquakes, which were identified and classified in previous studies[30,38,41,53]. The waveforms were downloaded from the reported signal onset to 600 s afterward to ensure the inclusion of the *S*-wave arrival.

Then, the arrival time of the direct *S* wave in each unstacked event waveform was determined using waveform cross-correlation. We used stacked waveforms from Yosio Nakamura's dataset as templates, given their superior quality compared with the other two datasets (**Extended Data Fig. 2** versus **Extended Data Fig. 3 and 4**). Moreover, the consistency of relative spectral ratios across the datasets (**Extended Data Fig. 5**) suggests that the choice of template likely has minimal influence on the results. For each deep moonquake with a reliable location and a high-SNR stacked waveform (>6.0 dB), we extracted a 110-second window (10 s before to 100 s after the direct *S*-wave arrival) from the corresponding stacked trace. Cross-correlation with the

unstacked waveform was then performed to determine the *S*-wave arrival time. Unstacked waveforms were retained only when both horizontal components exhibited cross-correlation coefficients greater than 0.1 and when the time shifts corresponding to their peak correlations were consistent. This criterion helps to filter out most misclassified or low-quality events listed in the catalog. A representative example is shown in **Extended Data Fig. 13**, which demonstrates that this method successfully retrieves direct *S* waves from unstacked waveforms. A few lower-quality events remain present, but these will be subsequently removed through SNR screening.

Next, we removed the instrumental response from the unstacked waveforms. Based on the response modes (Peak or Flat) of the Apollo lunar seismometer[50] associated with each waveform, we removed the corresponding instrumental response and converted the raw data to the ground velocity records. As can be seen in **Extended Data Fig. 14**, the dominant peak near 0.45 Hz in the Peak mode disappears following correction.

After that, we calculated the spectral ratio of each unstacked deep moonquake waveform. Without response correction, the stable frequency range can extend up to 2.0 Hz. However, once the response is removed, the low sensitivity of the Apollo seismometer at high frequencies[50] (> ~1.2 Hz) leads to anomalous amplification above that. To avoid this artifact, we limited the upper bound of the frequency band to 1.0 Hz when computing the spectral ratios. Testing the upper frequency limit of 1.0 Hz in the stacked waveform demonstrates that it would produce a similar spectral ratio distribution pattern (**Extended Data Fig. 9**).

We then computed the average spectral ratio for each cluster by taking the mean of all unstacked waveforms with an SNR greater than 4.0, 5.0, and 6.0 dB (**Extended Data Fig. 15, 16, and 17**). Due to the generally low SNR of unstacked data, the spectral ratios of individual events may fluctuate with the chosen SNR threshold. Nevertheless, the overall spatial pattern remains consistent at each station: at Apollo 12, events from the northeast and north yield relatively Low-frequency waveforms, whereas those from the southwest produce relatively High-frequency waveforms; at Apollo 15, relatively Low-frequency events originate from the south, while relatively High-frequency ones from the east; and at Apollo 16, events from the west are relatively Low-frequency, while those from the northeast are relatively High-frequency. **Extended Data Fig. 18** presents examples of unstacked waveforms, which align with the relatively Low- and High-frequency events identified in the stacked waveforms (**Fig. 2** in the Main text).

In addition, spectral ratios measured from individual unstacked waveforms are highly stable, with twice the standard deviation typically below 0.05 (e.g., **Extended Data Fig. 19**). This stability rules out the possibility that periodic tidal effects are responsible for relatively Low- and High-frequency characteristics in the stacked waveforms.

The most robust set of station-event pairs can be obtained by applying stringent selection criteria that require consistent spectral ratios across various parameter tests on stacked waveforms, as well as additional verification using unstacked data. At Apollo 12, relatively Low-frequency events include A6, A18, A20, and A25, while relatively High-frequency events include A1, A8, and A30. At Apollo 15, A1 is classified as relatively low-frequency, whereas A6 and A7 are relatively High-frequency. At Apollo 16, relatively Low-frequency events include A1, A8, A11, A14, A18, A20, A30, and A34, while A6, A7, and A25 are relatively High-frequency. Although this stringent screening yields fewer station-event pairs, it clearly reveals the raypath dependence for the waveform frequency contents of deep moonquakes (**Extended Data Fig. 20**).

References in the Methods

50. Nunn, C. *et al.* Lunar Seismology: A Data and Instrumentation Review. *Space Sci Rev* **216**, 89 (2020).
51. Liu, X., Xiao, Z., Li, J. & Nakamura, Y. Newly Discovered Temperature-Related Long-Period Signals in Lunar Seismic Data by Deep Learning. *Earth and Space Science* **11**, e2024EA003676 (2024).
52. Nunn, C., Nakamura, Y., Kedar, S. & Panning, M. P. A New Archive of Apollo's Lunar Seismic Data. *Planet. Sci. J.* **3**, 219 (2022).
53. Bulow, R. C., Johnson, C. L., Bills, B. G. & Shearer, P. M. Temporal and spatial properties of some deep moonquake clusters. *J. Geophys. Res.* **112**, 2006JE002847 (2007).

Acknowledgements

J.L. acknowledges support from the National Key R&D Program of China (Grant No. 2024YFF0809900), the National Natural Science Foundation of China (42474226, 42441827). We thank T. Wang, C.R. Han, Z.R. Zhang, and W.B. Zhang for their valuable discussions.

Author contributions

J.S. and J.L. designed the project. J.S. and J.L. conducted the main investigation. All authors participated in the analysis of the lunar evolution model. J.S. drafted the manuscript. J.S. produced all figures. All authors revised the manuscript.

Data availability

All the data used in this study are publicly available and appropriately cited throughout the text.

Code availability

All data and code to reproduce the figures in the main text are available in the Zenodo repository at (https://doi.org/10.5281/zenodo.16313727).

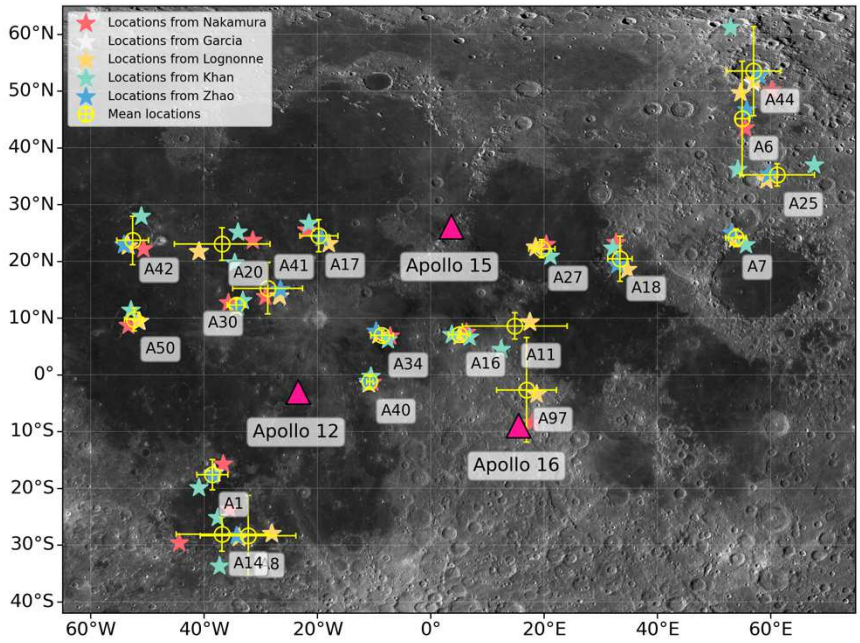
Competing interests

Authors declare that they have no competing interests.

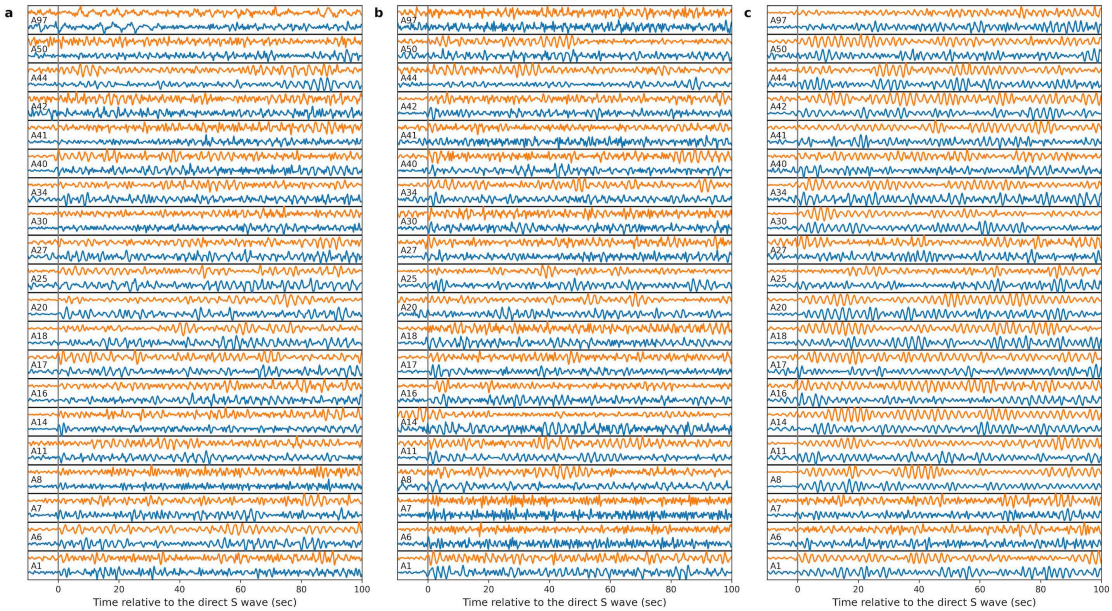
Supplementary information

Supplementary Materials S1, and Tables S1 and S2.

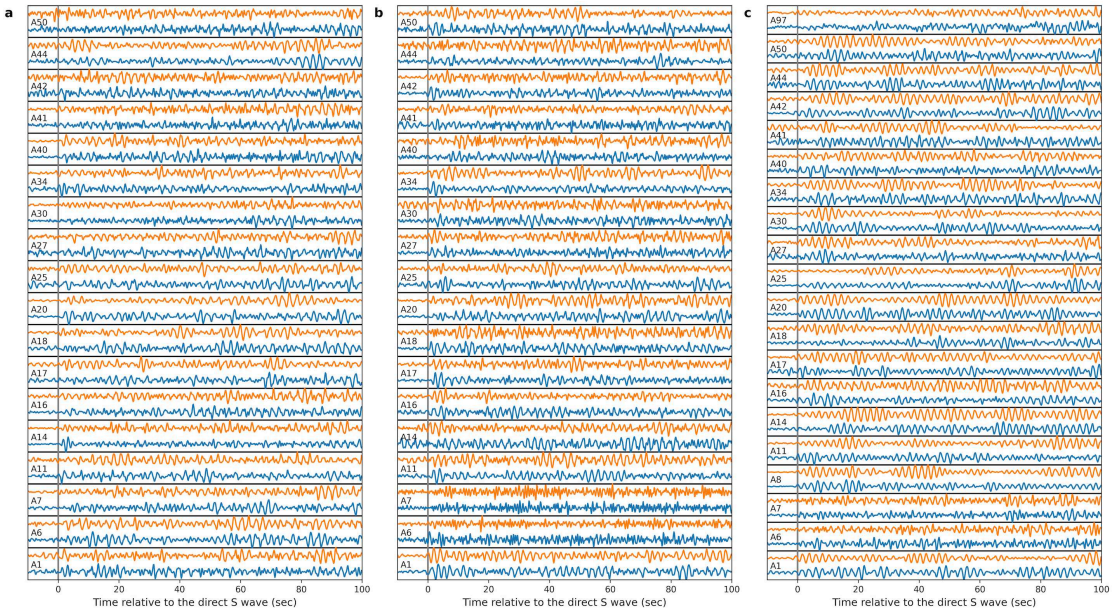
Extended Data



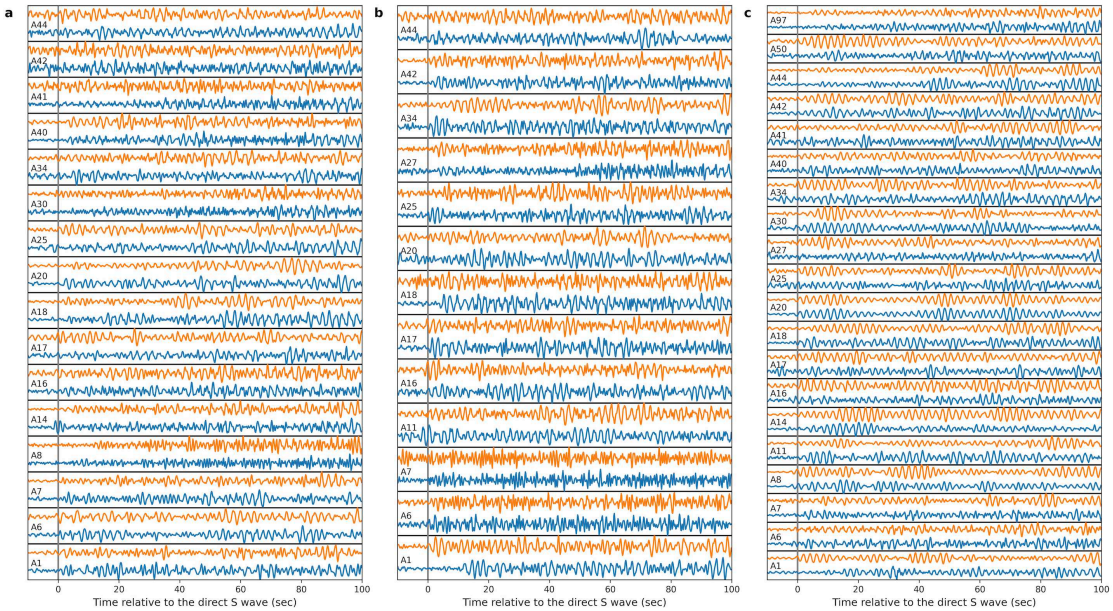
Extended Data Fig. 1 | Distribution of deep moonquakes with well-constrained locations. Coloured stars mark locations reported by different studies[30–34]. A location is considered well-constrained if at least four studies provide consistent results. Yellow circles with error bars indicate the mean location and associated uncertainty (twice the standard deviation) for each event. Event names are labelled at their corresponding positions, following the naming convention of previous work[40]. Pink triangles denote the positions of the Apollo 12, Apollo 15, and Apollo 16 stations.



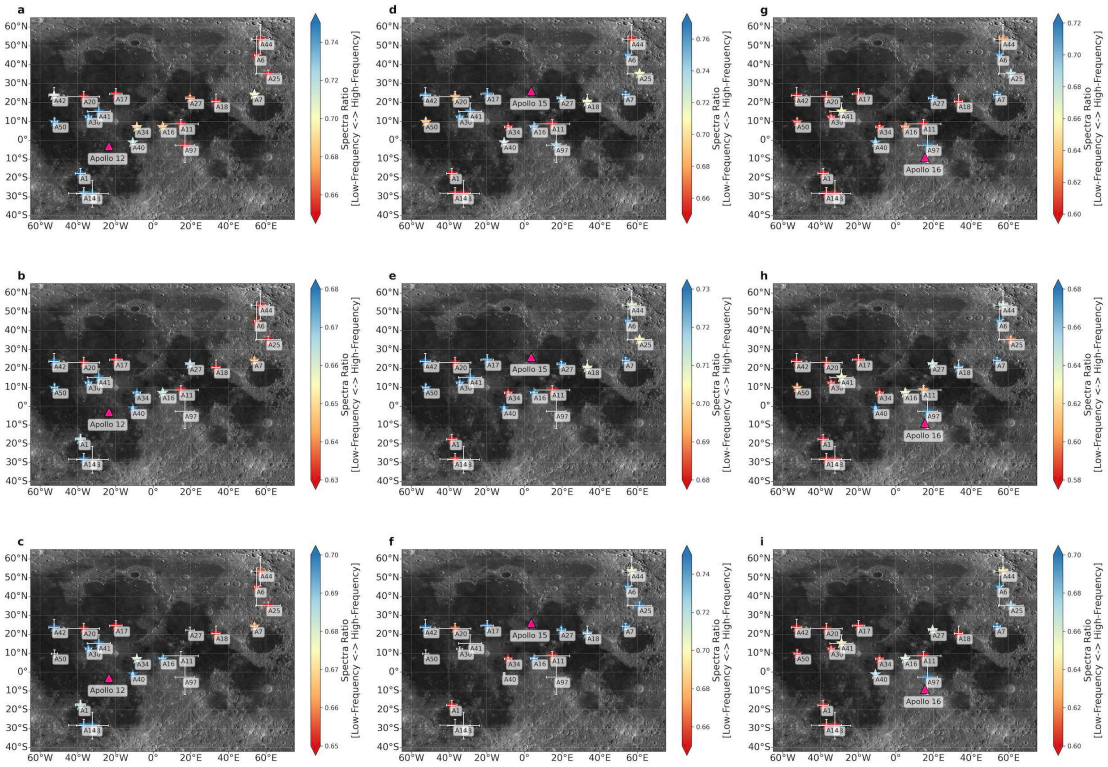
Extended Data Fig. 2 | Stacked waveforms of deep moonquakes with well-constrained locations recorded by the Apollo 12 (a), Apollo 15 (b), and Apollo 16 (c) stations. These stacks were compiled by Yosio Nakamura[40]. The X-axis shows time relative to the arrival of the picked direct *S* wave, with the gray vertical line indicating zero time. In each panel, the blue and orange lines represent the northern and eastern components, respectively. Waveforms were bandpass filtered between 0.05 and 2.5 Hz. The corresponding deep moonquake name is labelled on the left side of each waveform set.



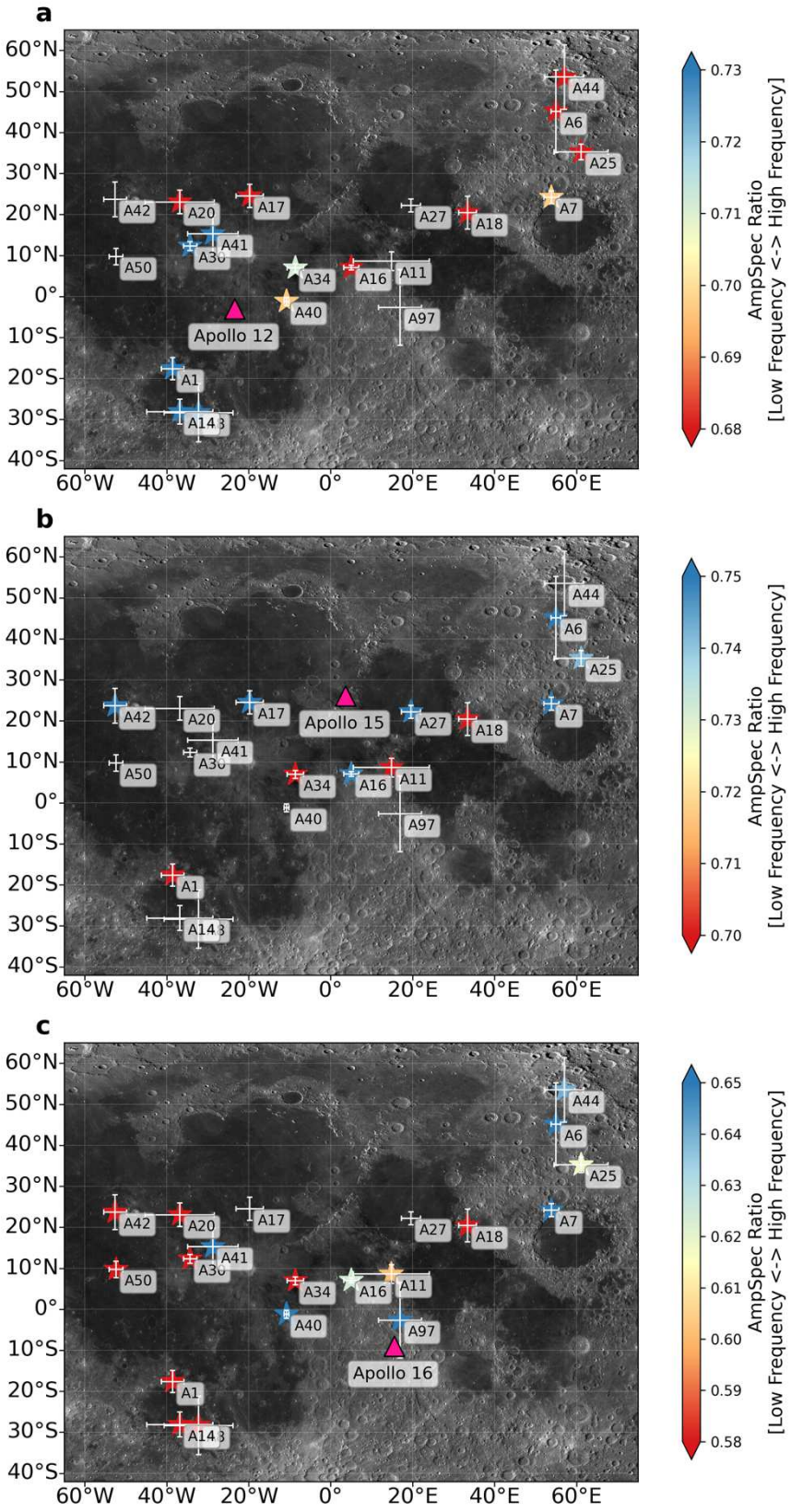
Extended Data Fig. 3 | Refer to Extended Data Fig. 2 for the caption. These stacks were compiled by Philippe Lognonné[40].



Extended Data Fig. 4 | Refer to Extended Data Fig. 2 for the caption. These stacks were compiled by Renee C. Bulow[40].

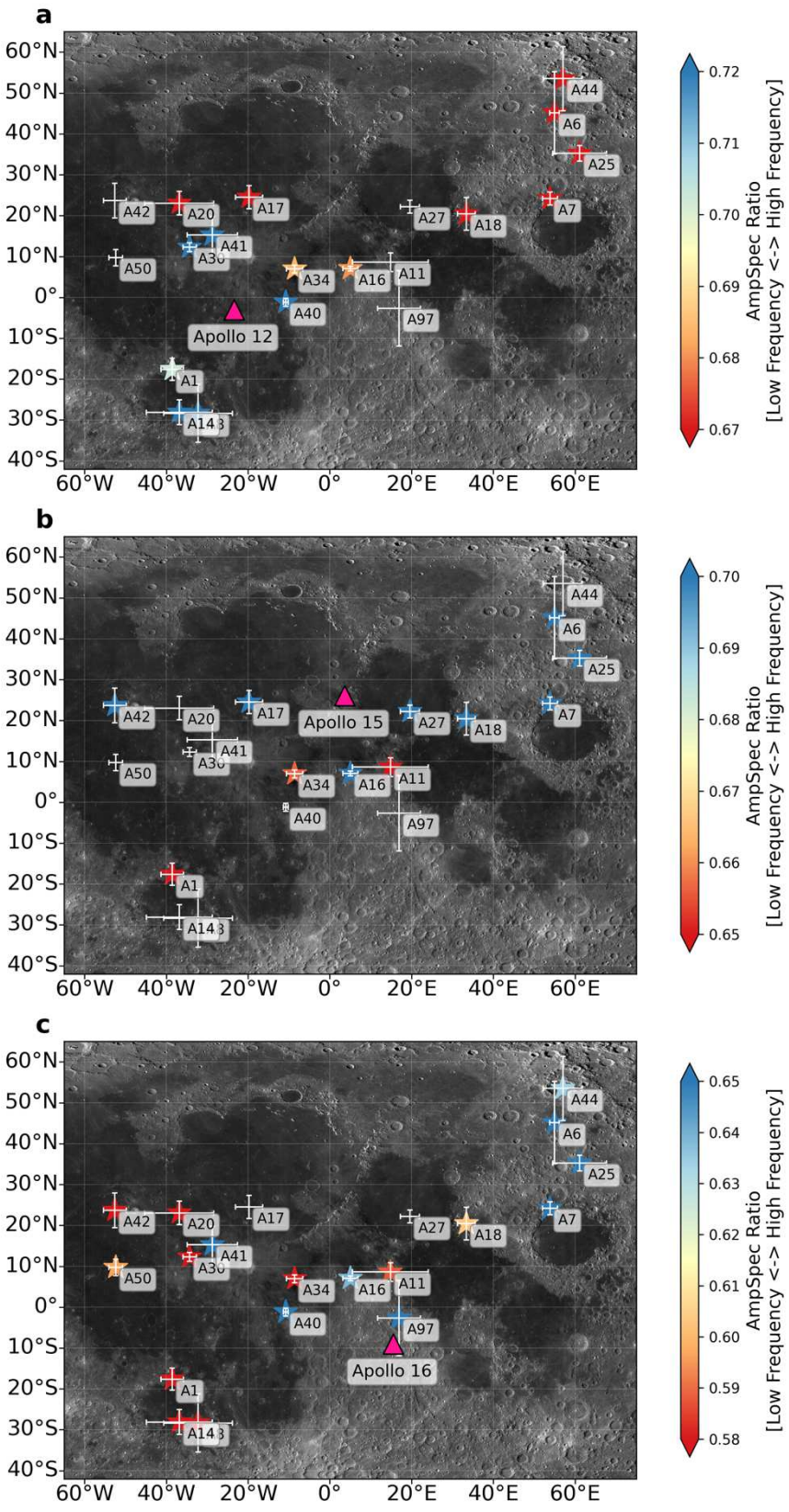


Extended Data Fig. 5 | Spatial distribution of relatively Low- and High-frequency deep moonquake events recorded at the Apollo 12 (a – c), Apollo 15 (d – f), and Apollo 16 (g – i) stations. The spectral ratios in the first, second, and third rows were derived from stacked waveform datasets compiled by Yosio Nakamura (**Extended Data Fig. 2**), Philippe Lognonné (**Extended Data Fig. 3**), and Renee C. Bulow (**Extended Data Fig. 4**), respectively. White crosses with error bars mark the locations of deep moonquakes with well-constrained positions (see **Extended Data Fig. 1**). Coloured filled stars represent individual events, with the colour indicating the spectral ratio. The redder colours correspond to lower-frequency waveforms, and bluer colours to higher-frequency waveforms. Areas without circles indicate locations where the corresponding stacked waveform is unavailable or of insufficient quality to identify the direct *S* wave, thus preventing the spectral ratio calculation.

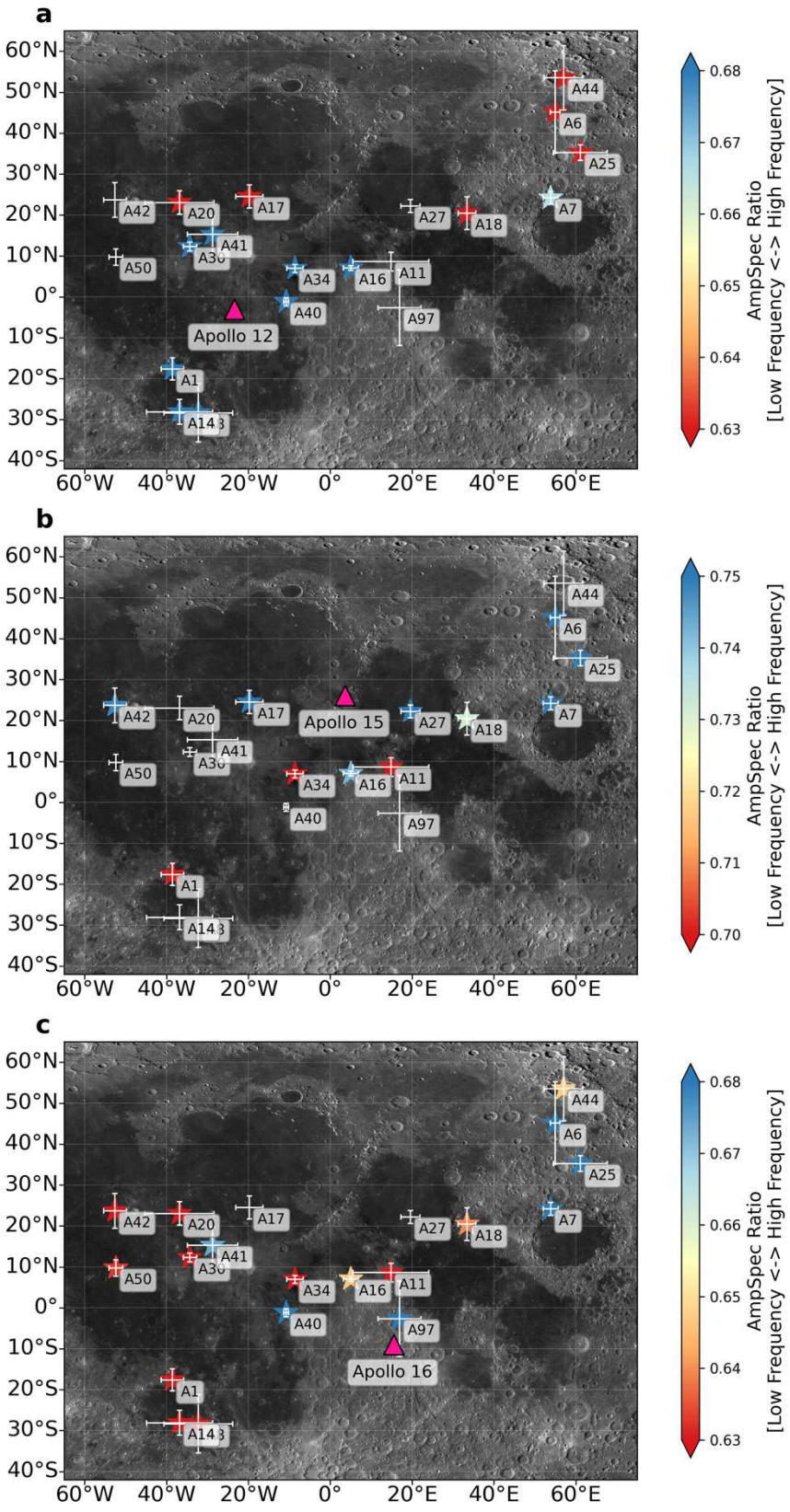


Extended Data Fig. 6 | Spectral ratio distributions of deep moonquake events at the Apollo 12 (a), Apollo 15 (b), and Apollo 16 (c) stations. The spectral ratios were calculated using a time window ranging from 10 s before to 50 s after the direct *S*-wave arrival, and a frequency band of 0.2 – 2.0 Hz. For each event, the spectral ratio

661 represents the average of the high-SNR waveforms from at least two independent
662 stacked waveform datasets. White crosses with error bars mark events with reliable
663 location estimates (see **Extended Data Fig. 1**). Coloured stars denote individual events,
664 with redder colours indicating lower-frequency waveforms and bluer colours indicating
665 higher-frequency ones. Events without projected stars lack reliable spectral ratio
666 estimates due to poor waveform quality or low SNRs.
667

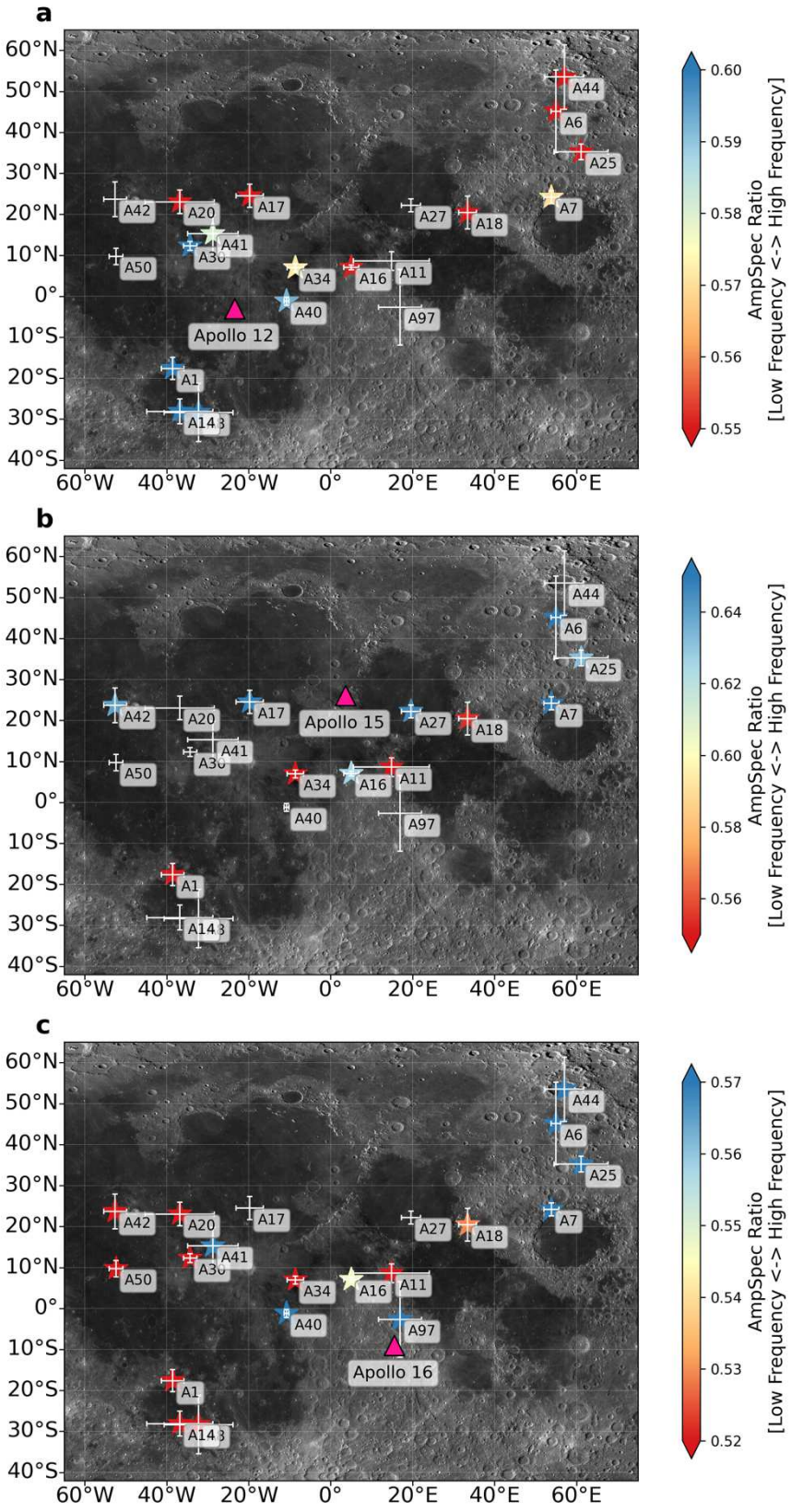


Extended Data Fig. 7 | Spectral ratio distributions of deep moonquake events recorded at the Apollo 12 (a), Apollo 15 (b), and Apollo 16 (c) stations. The spectral ratios were calculated using a time window ranging from 10 s before to 100 s after the direct *S*-wave arrival, and a frequency band of 0.2 – 2.0 Hz. Remaining legend details are as described in **Extended Data Fig. 6**.

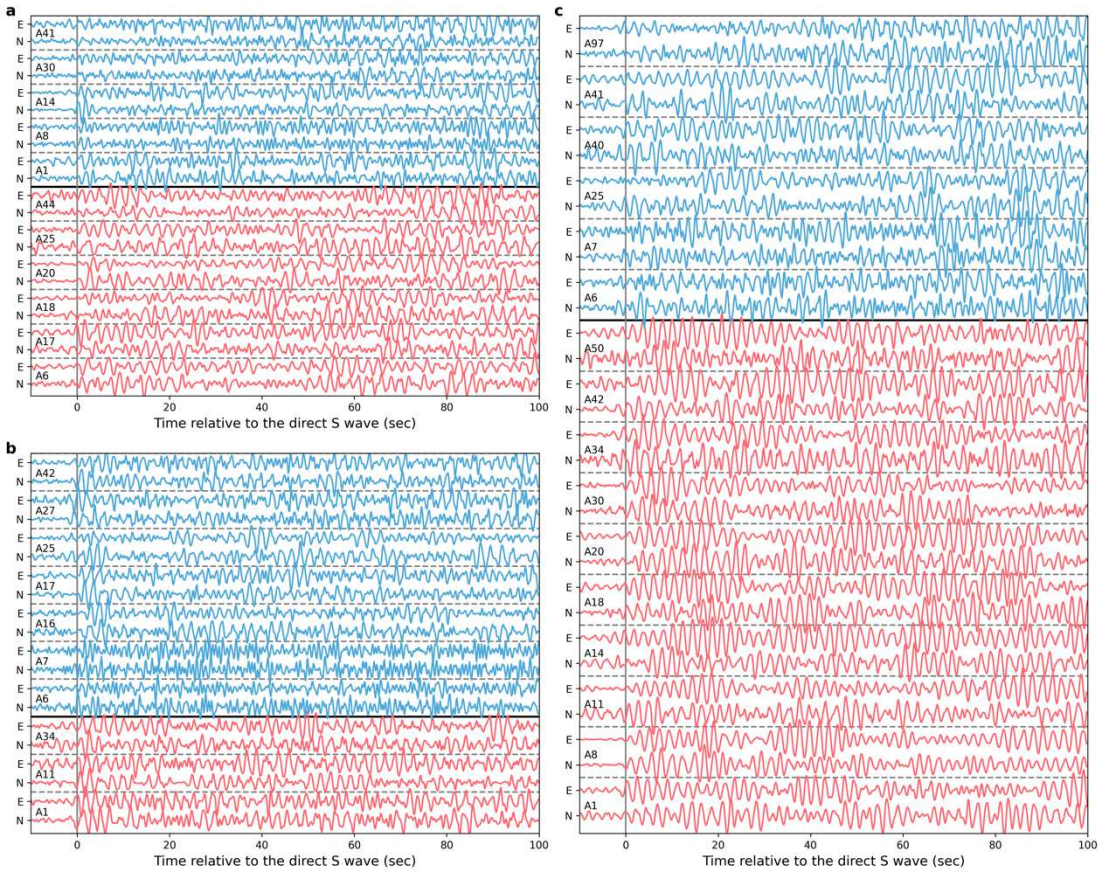


674

675 **Extended Data Fig. 8 | Spectral ratio distributions of deep moonquake events**
676 **recorded at the Apollo 12 (a), Apollo 15 (b), and Apollo 16 (c) stations.** The spectral
677 ratios were calculated using a time window ranging from 10 s before to 150 s after the
678 direct *S*-wave arrival, and a frequency band of 0.2 – 2.0 Hz. Remaining legend details
679 are as described in **Extended Data Fig. 6**.



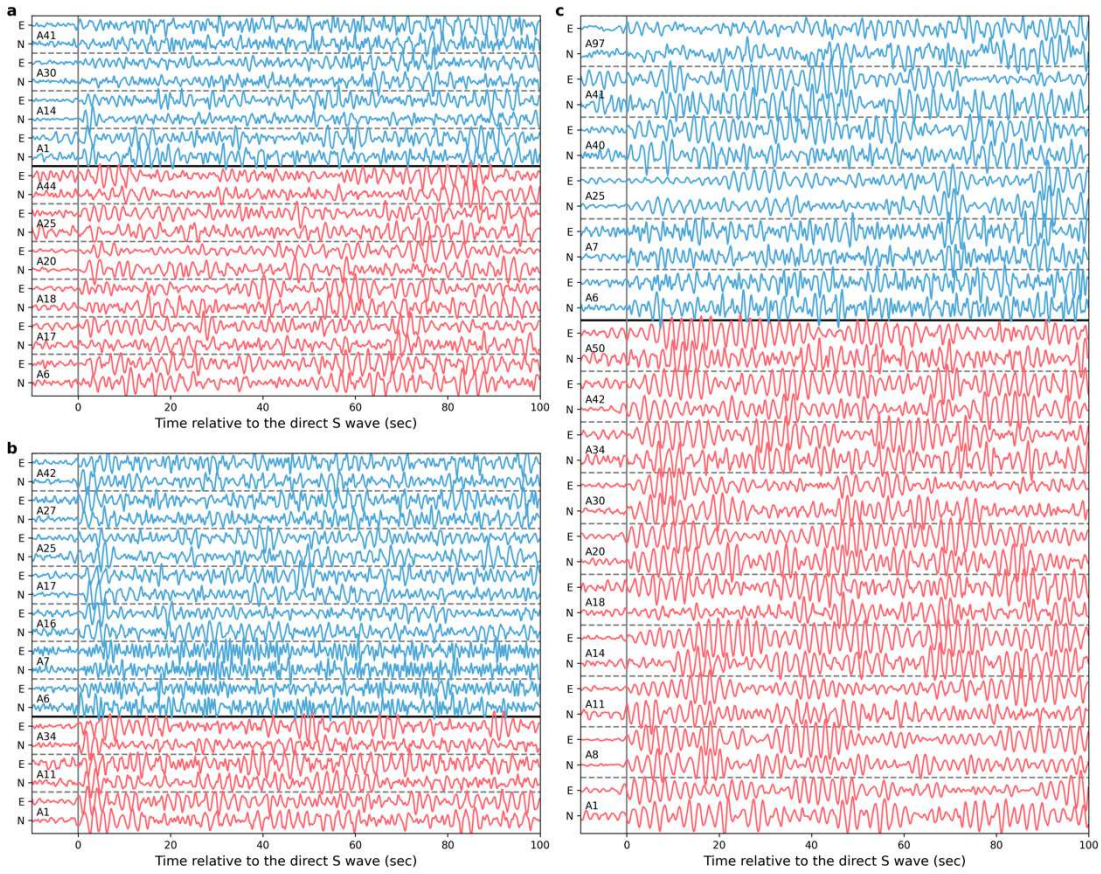
Extended Data Fig. 9 | Spectral ratio distribution of deep moonquake events recorded at the Apollo 12 (a), Apollo 15 (b), and Apollo 16 (c) stations. The spectral ratios were calculated using a time window ranging from 10 s before to 100 s after the direct *S*-wave arrival, and a frequency band of 0.2 – 1.0 Hz. Remaining legend details are as described in **Extended Data Fig. 6**.



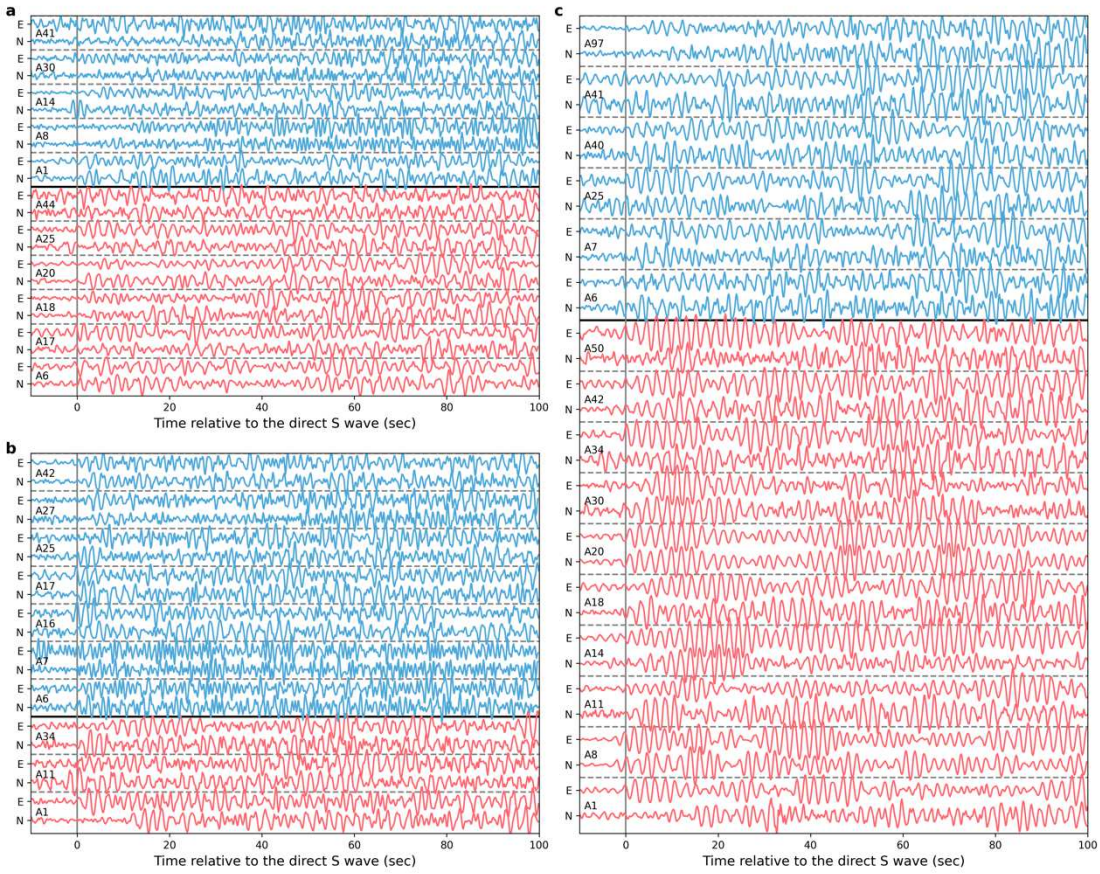
686

687 **Extended Data Fig. 10 | Stacked waveforms of relatively Low- and High-frequency**
688 **deep moonquake events recorded at the Apollo 12 (a), Apollo 15 (b), and Apollo 16**
689 **(c) stations.** The red and blue traces correspond to relatively Low- and High-frequency
690 events, respectively. These stacks are from the dataset of Yosio Nakamura[40]. All
691 waveforms are bandpass filtered between 0.05 – 2.5 Hz. The two horizontal
692 components (northern, N; eastern, E) are labelled to the left of each waveform set, along
693 with the corresponding event name. The X-axis shows time relative to the direct *S*-wave
694 arrival.

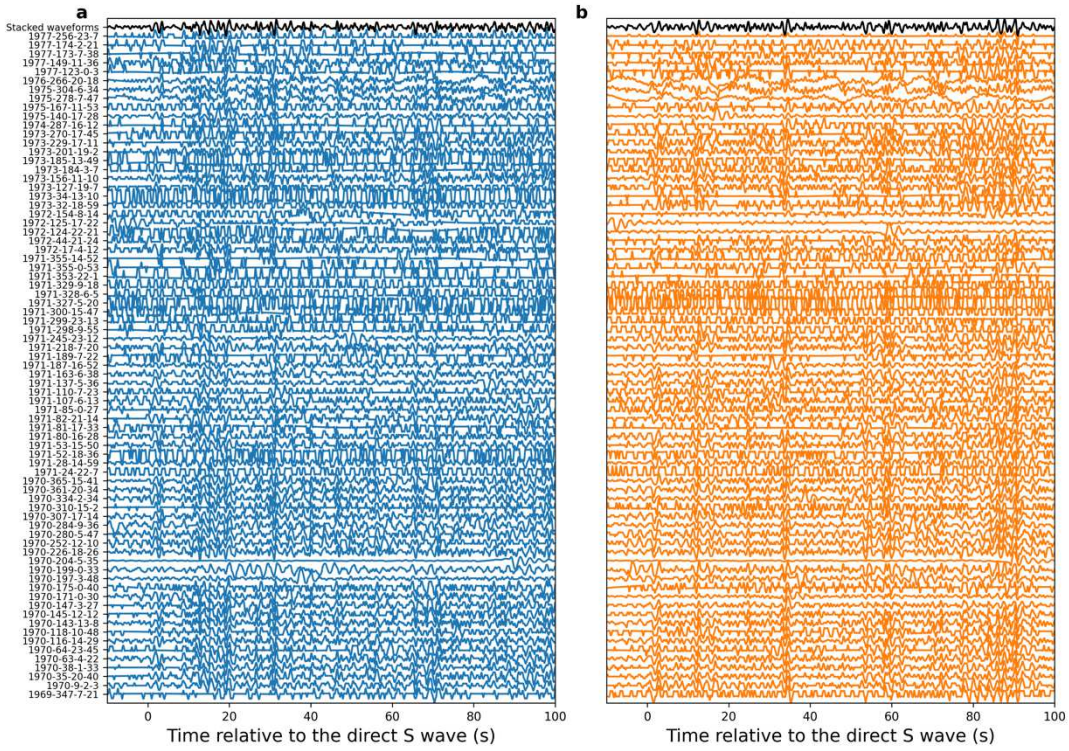
695



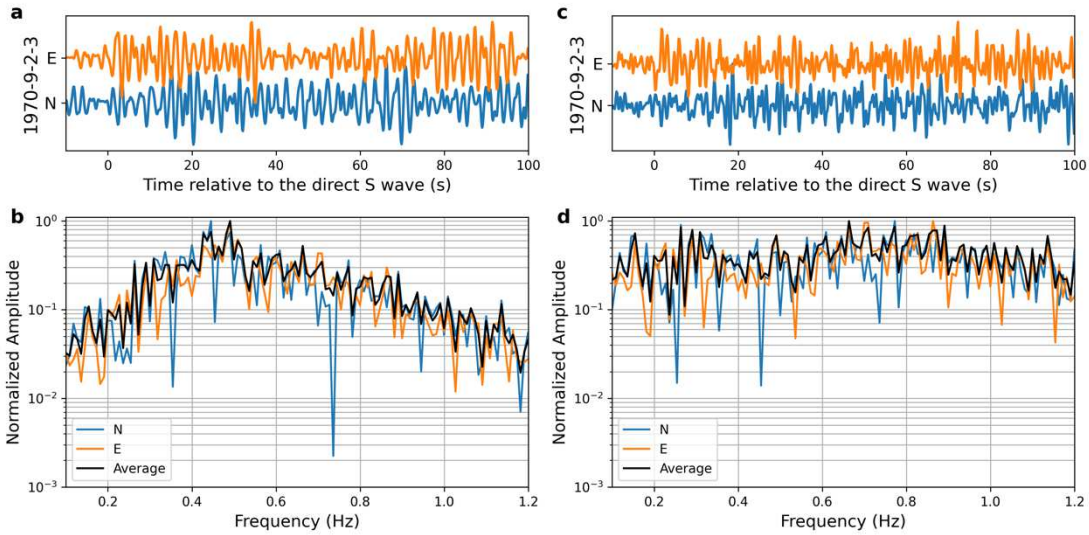
Extended Data Fig. 11 | Stacked waveforms of relatively Low- and High-frequency deep moonquake events recorded at the Apollo 12 (a), Apollo 15 (b), and Apollo 16 (c) stations. Waveforms are from the dataset compiled by Philippe Lognonné[40]. Refer to **Extended Data Fig. 10** for the caption.



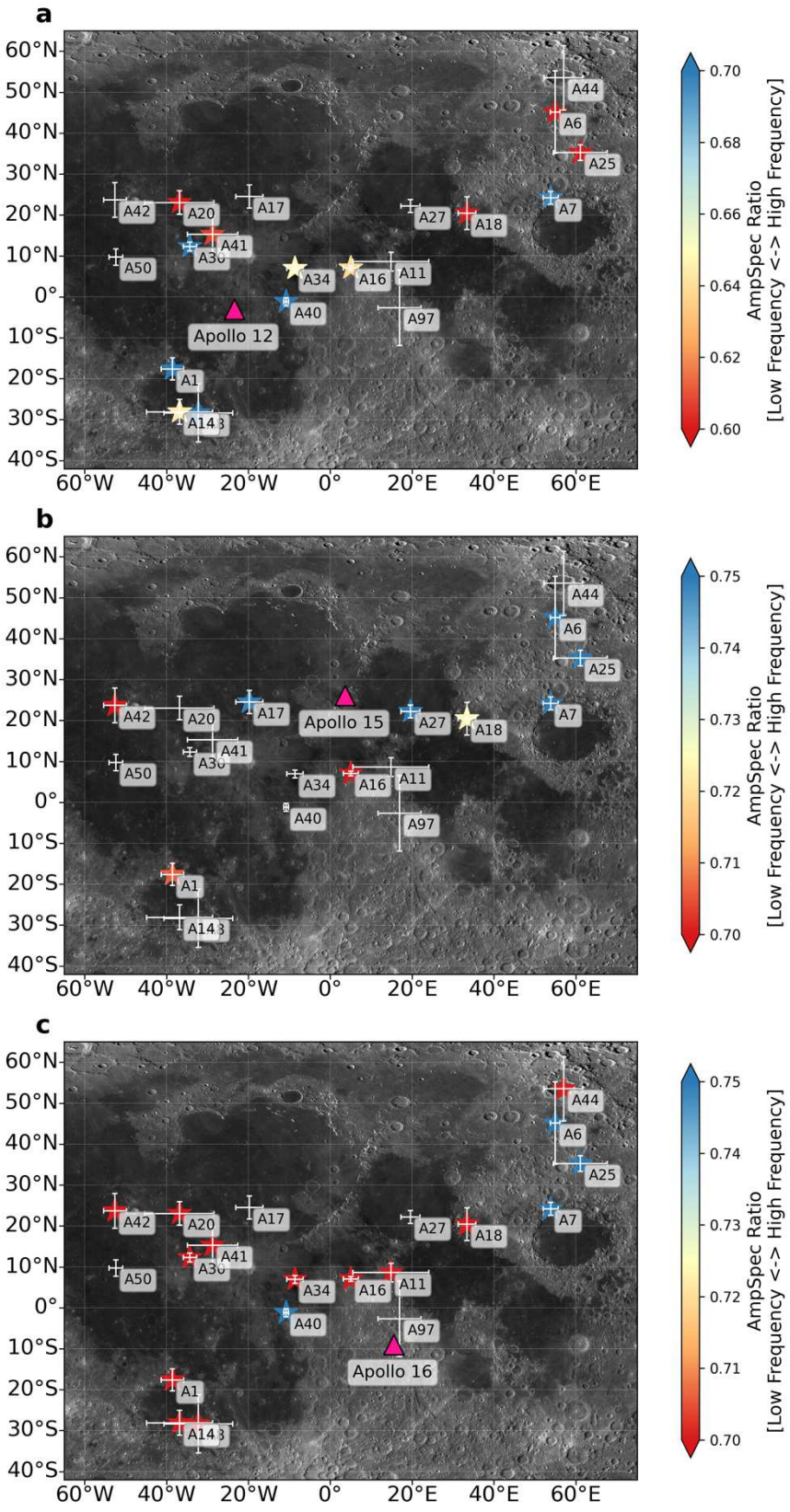
Extended Data Fig. 12 | Stacked waveforms of relatively Low- and High-frequency deep moonquake events recorded at the Apollo 12 (a), Apollo 15 (b), and Apollo 16 (c) stations. Waveforms are from the dataset compiled by Renee C. Bulow[40]. Refer to **Extended Data Fig. 10** for the caption.



Extended Data Fig. 13 | Direct *S*-wave seismograms of unstacked waveforms identified via cross-correlation. a, Waveforms in the northern component. **b**, Waveforms in the eastern component. The X-axis indicates time relative to the direct *S*-wave arrival. Each trace represents an individual unstacked waveform. The corresponding event name from the *levent.1008c* catalog[40] is labelled on the left (format: year-Julian day-hour-minute). All waveforms were bandpass filtered between 0.05 and 2.5 Hz. The template waveform used for cross-correlation is shown at the top.

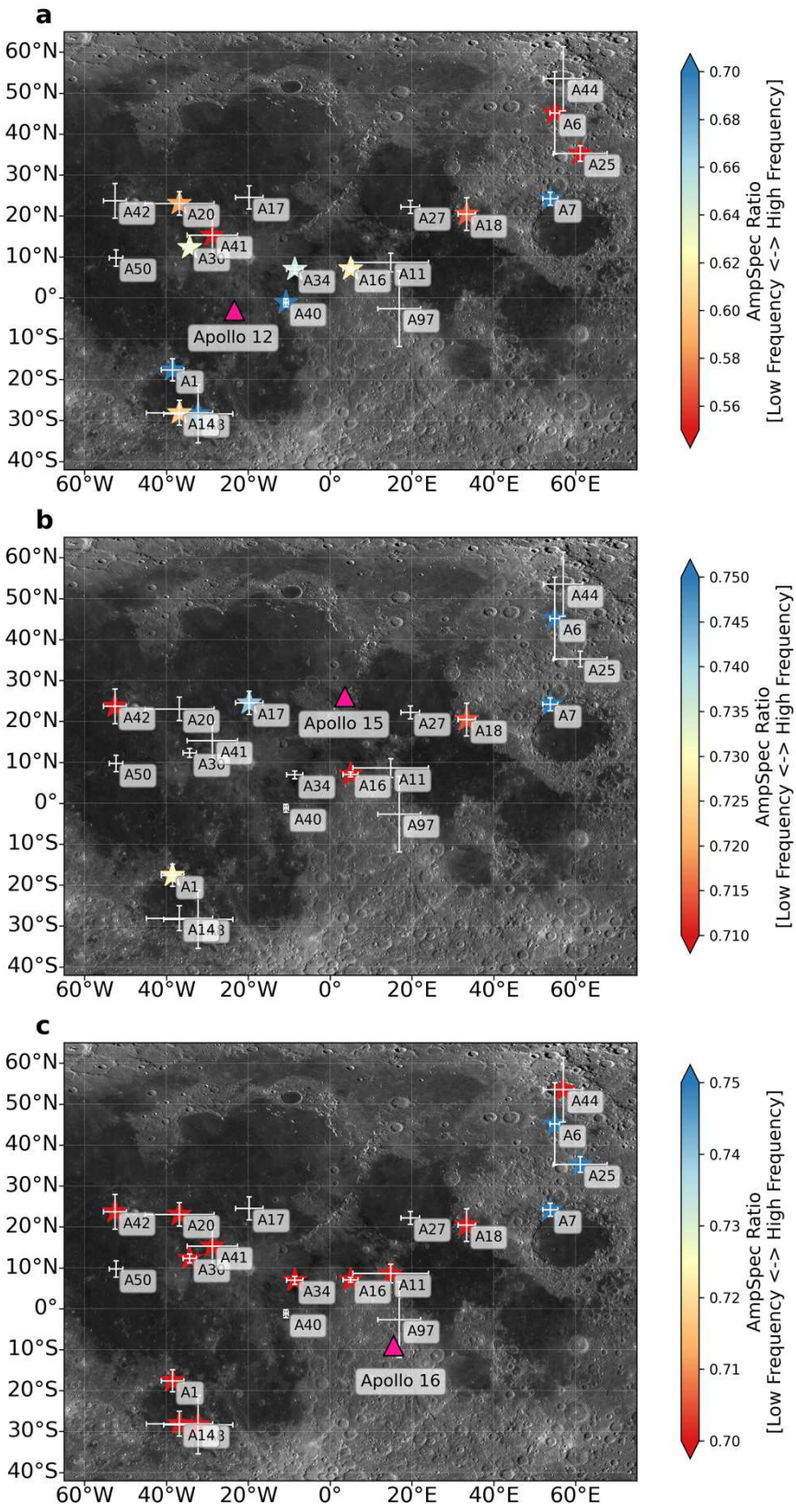


Extended Data Fig. 14 | Example of the instrumental response correction. a, Raw unstacked waveform of the 1970-09-02-03 event (formatted as year-Julian day-hour-minute; see *levent.1008c* catalog[40]), bandpass filtered to 0.1 – 1.2 Hz. The blue and orange traces represent the northern (N) and eastern (E) components, respectively. The X-axis indicates time relative to the direct *S*-wave arrival. **b**, Corresponding amplitude spectra. The blue and orange lines show the spectra of the two horizontal components, and the black line indicates their average. The pronounced peak near 0.45 Hz reflects the instrumental Peak-mode response. **c**, Same waveform as in **a**, after the instrumental response removal. **d**, Amplitude spectra of the corrected waveform in **c**, showing the disappearance of the 0.45 Hz peak after correction.

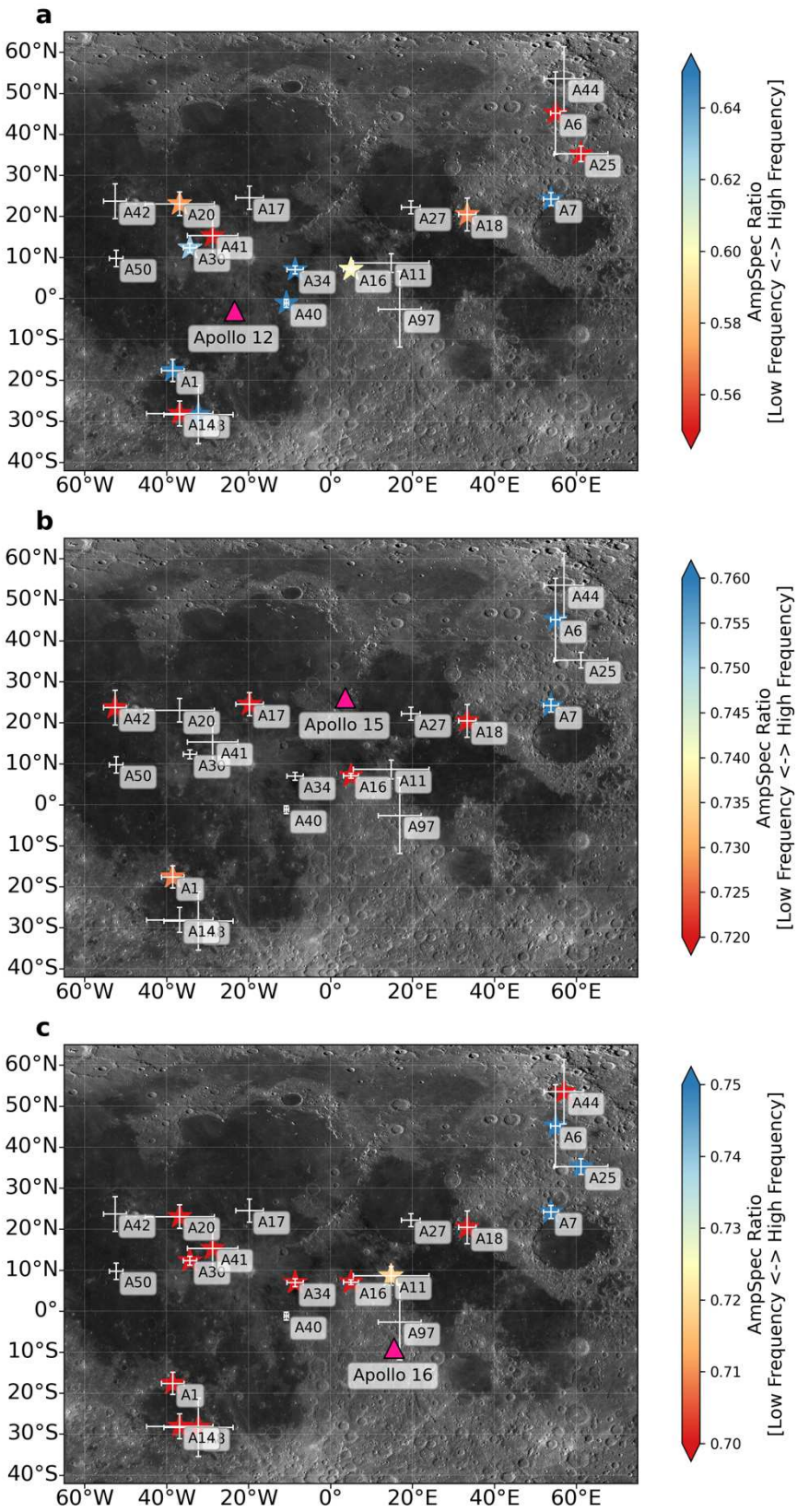


Extended Data Fig. 15 | Spectral ratio distributions of deep moonquake events recorded at the Apollo 12 (a), Apollo 15 (b), and Apollo 16 (c) stations. The spectral ratios were calculated from unstacked waveforms with direct *S*-wave signal-to-noise ratios exceeding 4.0 dB. The time window for computing the spectral ratios spans 10 s before to 100 s after the direct *S*-wave arrival, using a frequency band of 0.2 – 1.0 Hz.

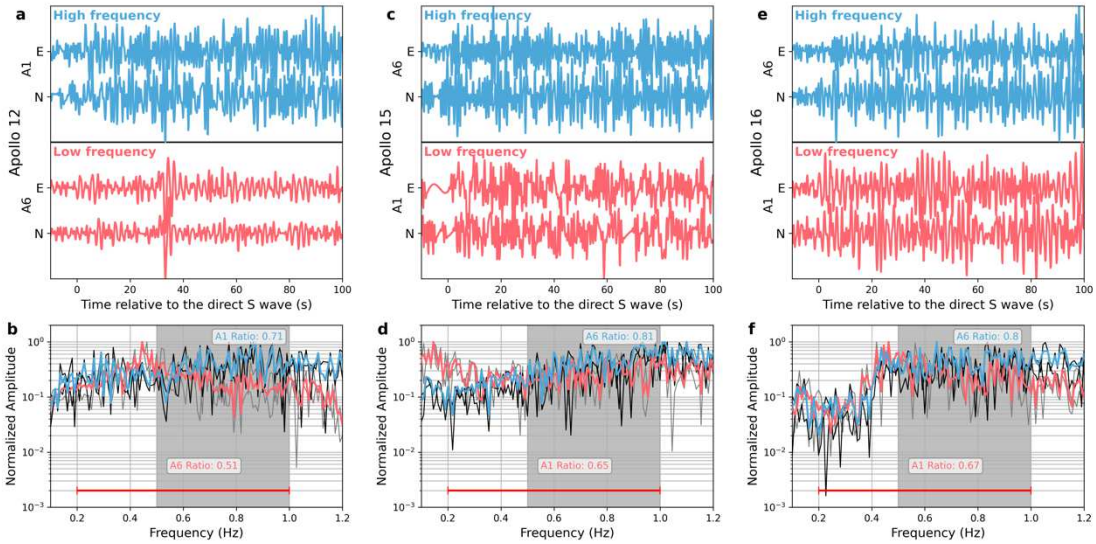
White crosses with error bars indicate events with well-constrained locations (see **Extended Data Fig. 1**). Coloured stars represent individual events, with redder ones indicating lower-frequency waveforms and bluer ones indicating higher-frequency ones. Events lacking projected stars have no reliable spectral ratio estimates due to low SNR or failure to match any unstacked waveform.



Extended Data Fig. 16 | Spectral ratio distributions of deep moonquake events recorded at the Apollo 12 (a), Apollo 15 (b), and Apollo 16 (c) stations. The spectral ratios were calculated from unstacked waveforms with direct *S*-wave signal-to-noise ratios exceeding 5.0 dB. The remaining legend details are as described in **Extended Data Fig. 15**.

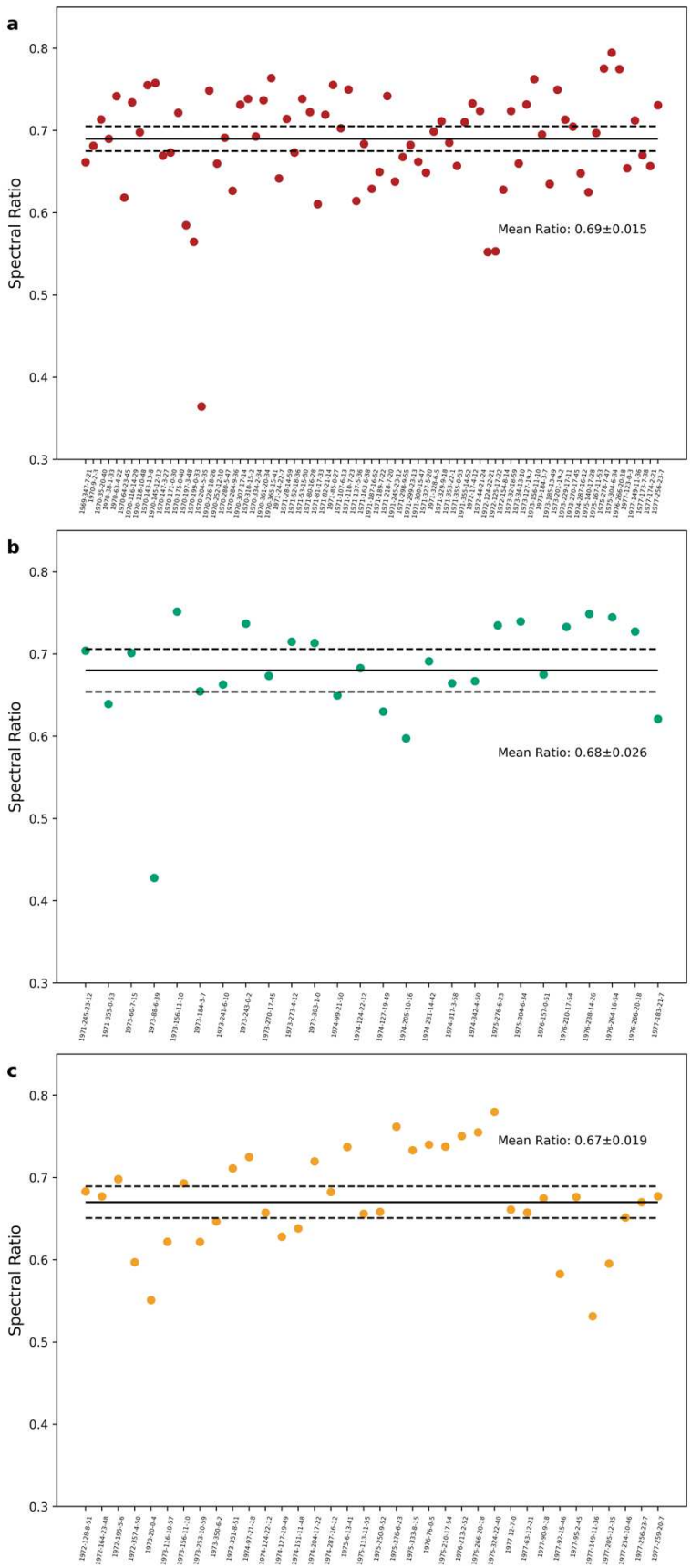


Extended Data Fig. 17 | Spectral ratio distributions of deep moonquake events recorded at the Apollo 12 (a), Apollo 15 (b), and Apollo 16 (c) stations. The spectral ratios were calculated from unstacked waveforms with direct *S*-wave signal-to-noise ratios exceeding 6.0 dB. The remaining legend details are as described in **Extended Data Fig. 15**.



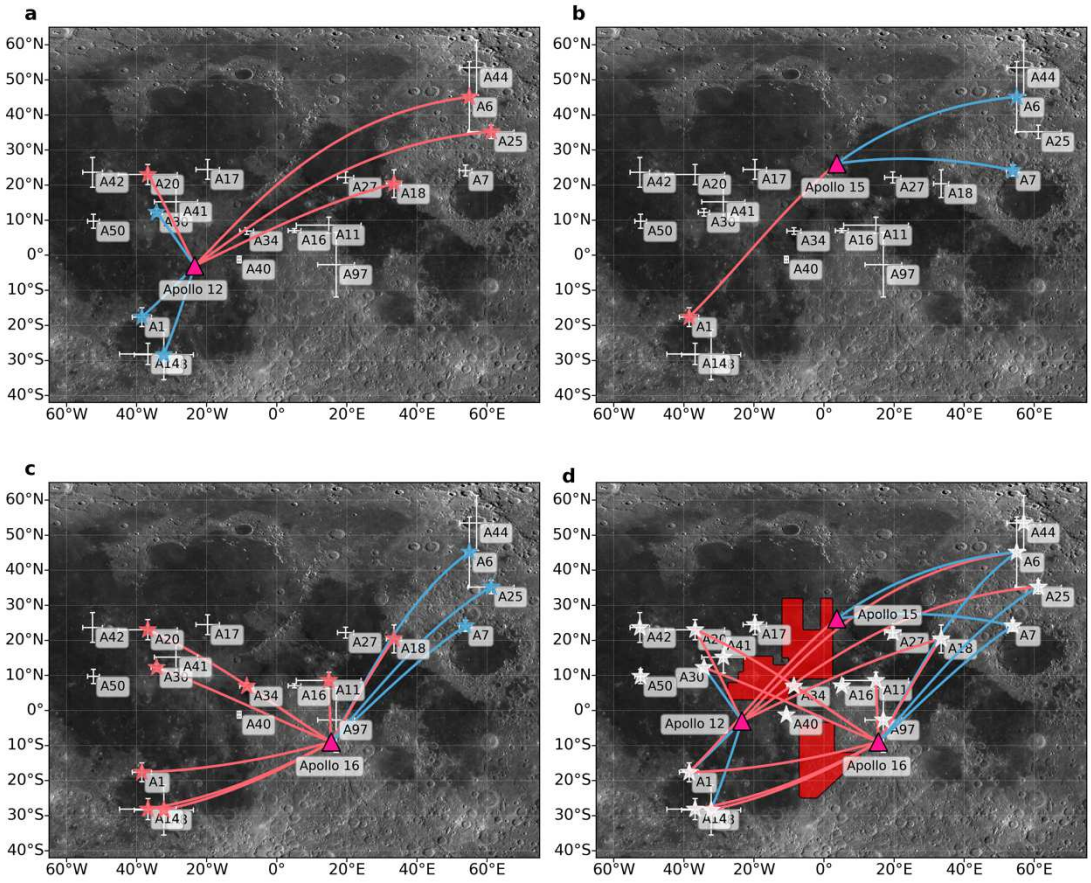
753

754 **Extended Data Fig. 18 | Examples based on unstacked waveforms of relatively**
755 **Low- and High-frequency deep moonquake events recorded at the Apollo 12 (a, b),**
756 **Apollo 15 (c, d), and Apollo 16 (e, f) stations.** All waveforms were corrected for
757 instrumental response and bandpass filtered between 0.1 and 1.2 Hz. **a,** Northern (N)
758 and eastern (E) components of events 1970-035-20-40 (cluster A1) and 1976-321-10-
759 50 (cluster A6) recorded at Apollo 12. The red and blue traces indicate relatively Low-
760 and High-frequency events, respectively. Event names follow the format year-Julian
761 day-hour-minute (see *levent.1008c* catalog[40]). Time is relative to the direct *S*-wave
762 arrival. **b,** Normalized amplitude spectra for the events in **a**. The gray and black lines
763 show individual spectra, and the red and blue lines denote their corresponding averages.
764 The spectral ratio values are annotated. **c, d,** As in **a** and **b**, for events 1974-099-21-50
765 (A1) and 1975-194-13-57 (A6) recorded at Apollo 15. **e, f,** As in **a** and **b**, for events
766 1977-256-23-07 (A1) and 1977-064-12-16 (A6) recorded at Apollo 16.
767

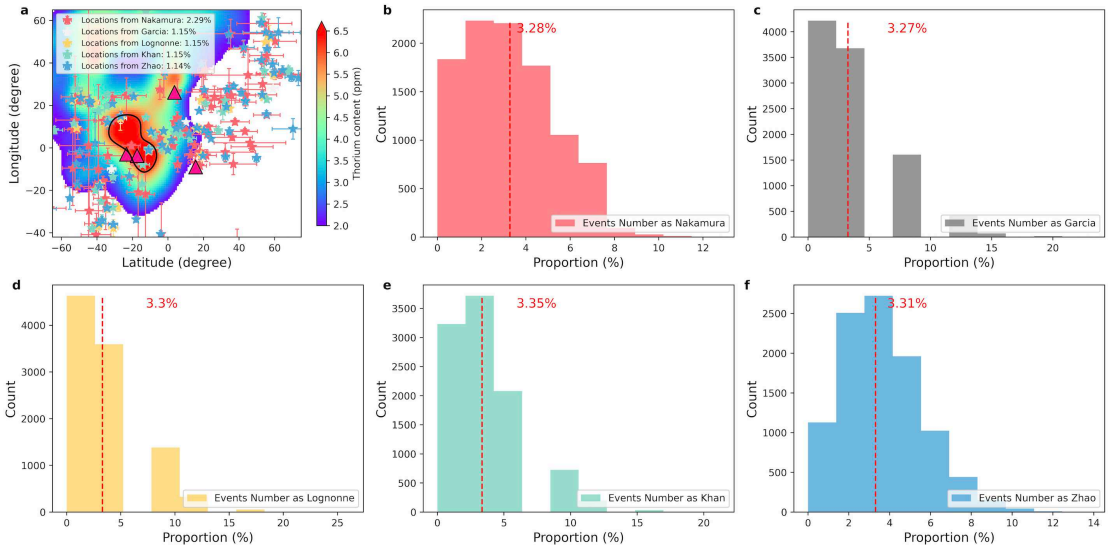


Extended Data Fig. 19 | Spectral ratio stability test for unstacked events at Apollo 12 (a), Apollo 15 (b), and Apollo 16 (c). All events belong to the A1 cluster. Each scatter point represents the spectral ratio of the direct *S*-wave from an individual

772 unstacked waveform. The X-axis shows event names in year-Julian day-hour-minute
773 format; the Y-axis indicates the measured spectral ratio. The solid black line denotes
774 the average spectral ratio, and the dotted lines mark twice the standard deviation based
775 on 10,000 bootstrap samples.
776

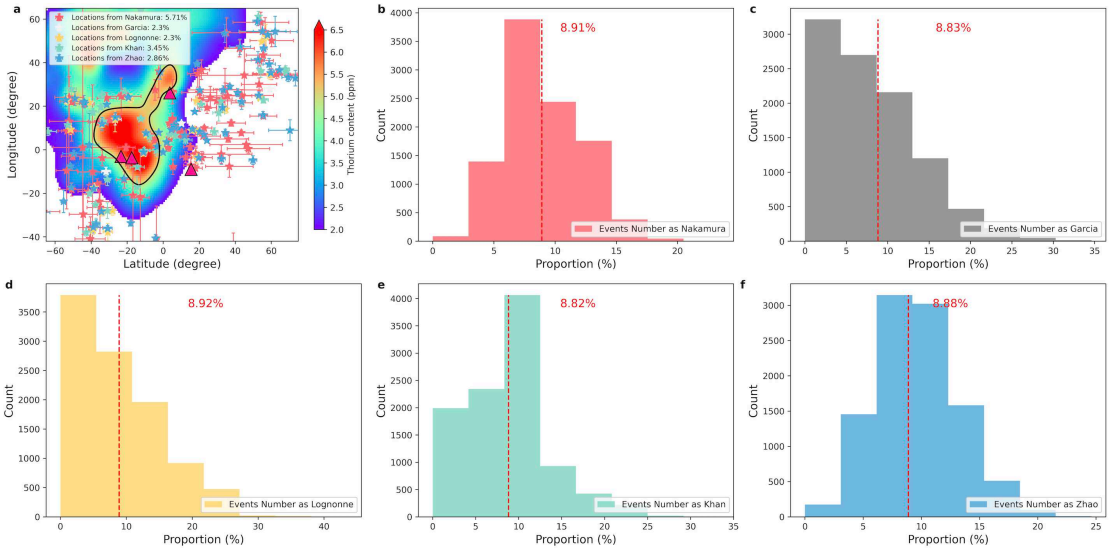


Extended Data Fig. 20 | Raypath projections of relatively Low- and High-frequency events recorded at the Apollo 12 (a), Apollo 15 (b), and Apollo 16 (c) stations. Event-station pairs are retained only if their spectral ratio classifications remain consistent across parameter variations in the stacked waveform analysis, and are further validated using unstacked waveforms. For complete caption information, refer to **Fig. 3** in the Main text.

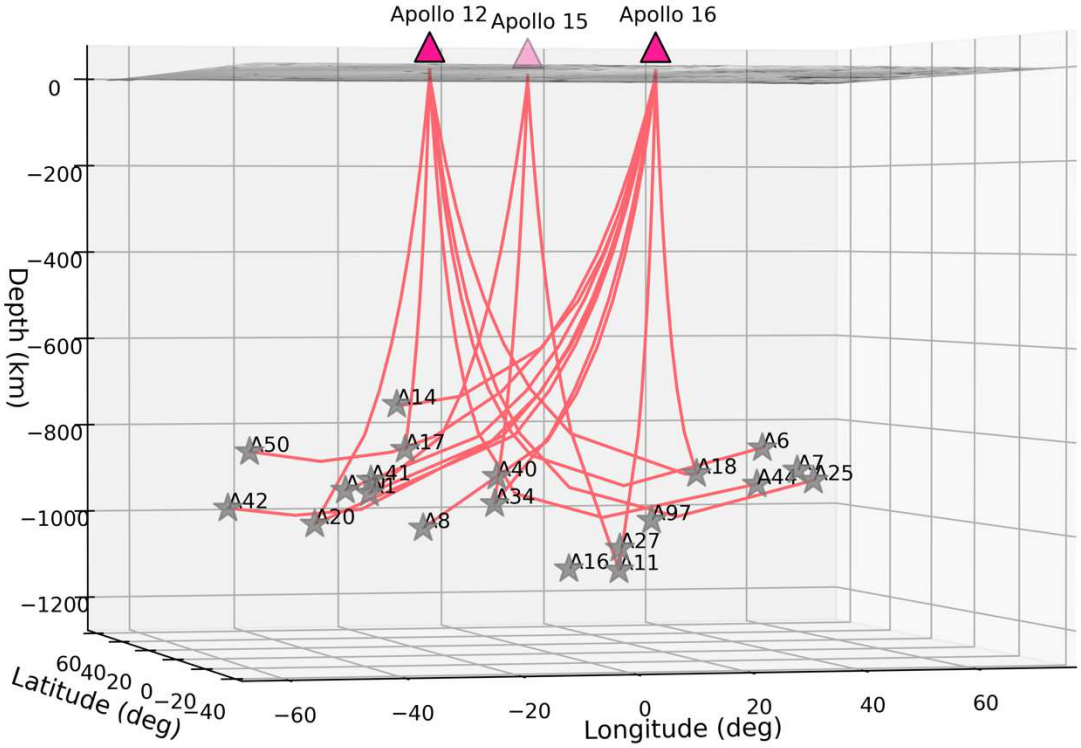


785

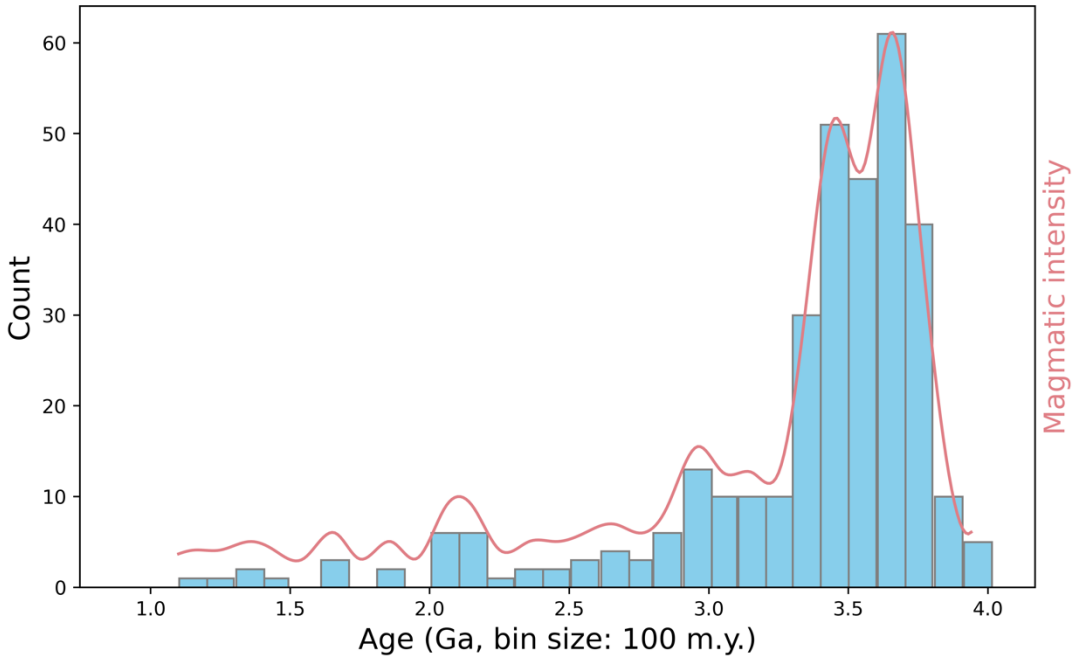
786 **Extended Data Fig. 21 | Statistical and simulation-based assessment of**
787 **distributions of deep moonquakes in thorium-rich regions (>6 ppm). a**, Distribution
788 of deep moonquakes from five independent catalogs[30–34] overlaid on the thorium
789 abundance map. The black contour outlines the 6-ppm threshold. Coloured stars denote
790 events from different catalogs, and pink triangles mark Apollo seismometer locations.
791 The upper-left inset shows the percentage of events falling within the >6 ppm region
792 for each catalog. **b – f**, Results of 10,000 random simulations for each catalog, showing
793 the expected proportion of events within the >6 ppm region if locations were randomly
794 distributed. The X-axis represents the proportion produced in each simulation, and the
795 Y-axis represents the number. The vertical red dashed line marks the average of all
796 simulations.



Extended Data Fig. 22 | Statistical and simulation-based assessment of the distributions of deep moonquakes in thorium-rich regions (>5 ppm). Caption details are as in **Extended Data Fig. 21**.



Extended Data Fig. 23 | Three-dimensional raypaths of direct *S* waves from identified relatively Low-frequency events to the Apollo stations. Gray stars mark the locations of all deep moonquakes with reliable positions, averaged across existing catalogs (**Extended Data Fig. 1**). Pink triangles indicate the three Apollo stations. Solid red lines represent *S*-wave raypaths from relatively Low-frequency events to the corresponding stations, calculated using the very preliminary reference Moon model [32].



Extended Data Fig. 24 | Age distribution of lunar mare basalts and the inferred magmatic activity intensity. The blue histogram depicts basalt ages compiled from ref. 19, with age (billion years ago, Ga) and sample count on the X- and Y-axes, respectively. The red curve denotes the relative intensity of magmatic activity, derived using cubic spline interpolation.

Supplementary Files

This is a list of supplementary files associated with this preprint. Click to download.

- SupplementaryMaterial.pdf